



UNIVERSITY OF
CAMBRIDGE

Department of Engineering

3D Printing of Multi-Material Hydrogels

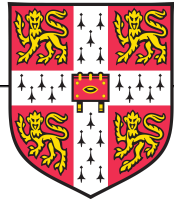
Author Name: Lorcan Nicholls

Supervisor: Yan Yan Shery Huang

Date: 29th May, 2024

I hereby declare that, except where specifically indicated, the work submitted herein is my own original work.

Signed _____ *Lorcan Nicholls* date _____ 29/05/2024



3D Printing of Multi-Material Hydrogels

IIB Project Final Report by

Lorcan Nicholls (ln356@cam.ac.uk)

University of Cambridge, Girton College

29th May, 2024

Senior Supervisor: Dr. Yan Yan Shery Huang

PhD Student Supervisor: Yaqi Sheng

Contents

① Technical Abstract	2	
② Introduction	4	
2.1. Background & Literature Review ..	4	
2.2. Project Scope	11	
③ Theory and Experiment Design	13	
3.1. Theoretical Treatment	13	
3.2. Design of Experiment	20	
④ Materials and Methods	22	
4.1. Apparatus	22	
4.2. Experimental Techniques	26	
⑤ Results and Discussion	30	
⑥ Conclusions	40	
6.1. Primary Findings	40	
6.2. Future Work	42	
⑦ References	46	
⑧ Appendix	48	
8.1. Appendix I: Abbreviations	48	
8.2. Appendix II: Hydrogel Moduli	49	
8.3. Appendix III: Robot Arm Code	50	
8.4. Appendix IV: Risk Assessment	51	

(1) Technical Abstract

3D Printing of Multi-Material Hydrogels

Lorcan Nicholls (ln356@cam.ac.uk), Girton College, University of Cambridge

Summary

The advent of hydrogels has revolutionised biomedical science, propelling research in bioengineering and nanoscience due to their mechanically flexible, soft, and biocompatible properties. While functional materials like magnets are ubiquitous, their integration with hydrogels into composite materials remains underdeveloped despite significant potential. This project presents the synthesis, optimisation, characterisation, and applications of 3D-printable magnetic nanofiber-hydrogel composites optimised for fatigue resistance. Two applications for these composites include substrates for *in vitro* lung organoids to study mechanobiological interactions of lung epithelial cells during inspiration via programmable electromagnets, and as tissue-mimetic fillers for post-surgical cavities to prevent internal tissue adhesions. Although these applications were outside the scope of the experimentals in this project, they are a key focus of the conclusions on this project's potential applications.

Report Structure

The report begins with a literature review of current magnetic soft actuator technology and microfiber synthesis, followed by a theoretical analysis of the target composite system. It details the experimental procedures for modular synthesis and provides a quantitative comparison of magnetic responsiveness across various material compositions. The report concludes with a discussion on the applications, advantages, and challenges of these materials.

Approach

Although stimuli-responsive pure hydrogels have been known in the literature for decades, these systems rely on their intrinsic physicochemical properties, such as the effect of environmental pH, temperature and light sensitivity on the hydrogel crosslinking and ionisation. These environmental parameters must be tightly controlled in the biomedical domain to maintain cell viability both *in vitro* and *in vivo*, limiting the utilisation of this mode of actuation in soft biocompatible materials. Magnetism, as a straightforward method for applying external, no-contact forces on soft materials, with manageable cytotoxicity, was chosen as a suitable functional material to enable actuation while maintaining a homeostatic environment. This led to the development of a composite of flexible magnetic-polymer microfibers within a hydrogel matrix for soft biocompatible actuators.

A theoretical framework based on structural analysis and multiphysics simulations guided the material selection process. Experiments identified fibres with optimal magnetic responsiveness and hydrogels with suitable viscoelastic and rheological properties. Wet spinning was used to produce the fibres, and 3D bioprinting to incorporate them into the hydrogel matrix (although manual extrusion is also possible and was simpler for demonstration purposes). The fibres were encapsulated within the hydrogel in its liquid phase and solidified by cooling. The composites were tested for deflection under a switching magnetic field, evaluating sensitivity and fatigue resistance.

Results

Automated wet spinning, using a robotic arm and motor-controlled spinner, produced fibres with consistent morphology. Light microscopy revealed an average fibre diameter of 15 ± 9 microns, largely independent of the synthesis formula. Iron oxide (Fe_3O_4) and polystyrene were used to create the magnetic-polymer fibres. A binary solvent of 85% *N,N*-dimethylformamide (DMF) and 15% acetone dissolved the mixture, producing fibres spun to an initial length of 28 mm. Variations in iron oxide and polystyrene concentrations (10%, 20%, 30% by weight) identified that a 40-50 wt% solid fraction yielded fully spinnable solutions, with highest magnetic responsiveness at the highest iron content. Deflection tests showed peak displacements of ~ 2 mm with virtually zero time lag or hysteresis, retained with the hydrogel. The 20% polystyrene and 30% iron oxide composition was optimal for fatigue resistance and hydrogel adherence, making it the optimal choice for soft actuators in remotely stimulated applications.

Conclusions

This project has demonstrated a novel synthesis of microfibre technology within soft biocompatible hydrogels with key challenges of such composites resolved, including fatigue resistance, prevention of delamination between the fibres, and prevention of cutting through the hydrogel during fibre actuation. The physical construction of the presented composite is straightforward and feasible with open-source technology, and is moreover expected to be highly biocompatible due to the separation between the inorganic magnetic fibre layer and the hydrogel in which cells may proliferate freely. This paves the way for soft actuator technology in a range of biomedical and nanoscience applications leveraging the inherent biocompatibility of the system.

② **Introduction**

2.1. Background & Literature Review

Materials designed to mimic the adaptability and flexibility of biological tissues hold immense promise for a variety of highly interdisciplinary science and engineering applications. In the recent decade, rapid progress in the fields of 3D and 4D bioprinting and responsive materials has led to the convergent development of soft functional materials which have driven research into current and emerging technologies including mechanobiology research, organoids, tissue engineering, regenerative medicine, actuators for soft robotics and smart textiles for wearable technology.

One of the key challenges relevant to many of these applications is the high standard of biocompatibility required of the constituent materials. In the realm of materials science, hydrogels occupy a distinct niche as a class of substances characterised by a cross-linked polymer network with the ability to absorb and retain substantial quantities of water, providing them with the properties of mechanical softness, flexibility, and biocompatibility [1]. While some shape-memory hydrogel formulations can be designed to exhibit an intrinsic response to stimuli such as light, temperature and pH on their own as a result of the steric and electrostatic properties arising from their physico-chemical bonding, their scope is broadened further when combined with other responsive materials, such as semiconductors [2], ferromagnets [3] [4] [5], ferroelectrics [6] and even superconductors [7]. These heterogeneous biphasic functional composites possess tunable properties by means of varying the morphology of the dispersed phase within the hydrogel into arrangements such as nanoparticles [8], nano- and microfibres, thin films and amorphous multi-material networks.

The present project undertakes an exploration into the potential of incorporating hydrogels into three-dimensionally printed magnetic composites for actuator applications. It is proposed that this synergistic combination of materials has the potential to yield actuators with enhanced performance and expanded functionality, while being manufacturable to high dimensional tolerance without the need for specialised fabrication facilities. A range of possible materials was surveyed based on both existing literature and new experimentation, and various important properties of interest of the resulting composites are characterised and reported. The exploration of 3D printing techniques for fabricating magnetic hydrogel composites offers precise control over the material's structure, shape, and functionality, unlocking new possibilities for complex and customized actuator designs. Through this research, we aim to contribute to the advancement of soft actuator technology by developing 3D printable magnetic hydrogel composites, opening up exciting opportunities for applications in diverse fields.

In this introductory section, a summary of the main principles behind the two core components of the new composite - **magnetic fibres** and **hydrogels** - is presented, followed by a literature review of the main fabrication techniques in the laboratory and their applications across science and engineering, and finally the scope of the project throughout its development is discussed.

Hydrogels

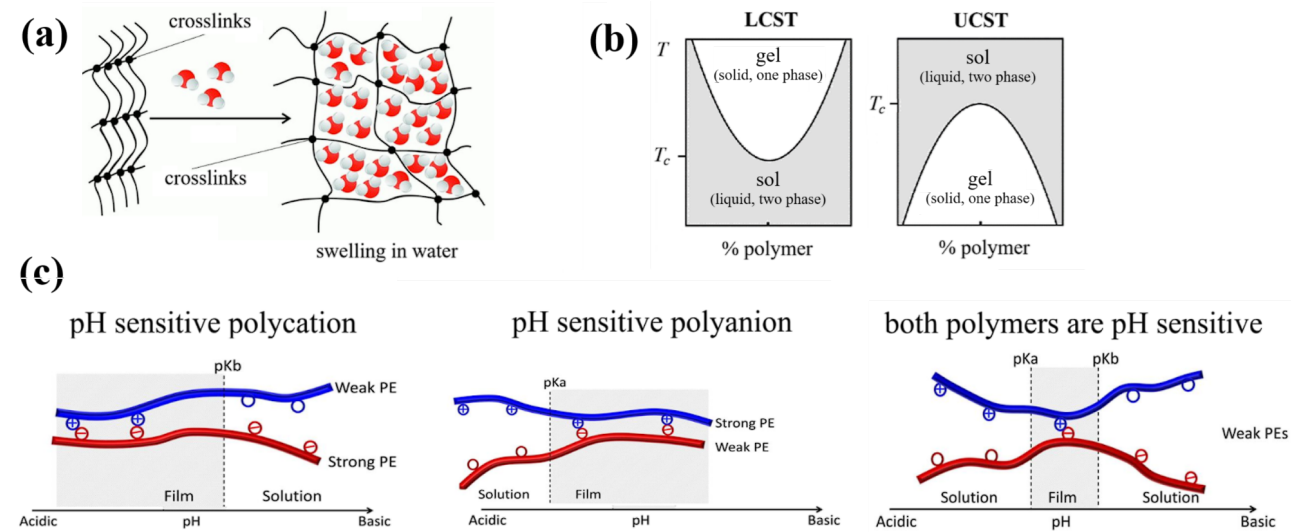


Fig. 1. Main principles of hydrogels. **(a)** Schematic of the swelling of crosslinked polymers due to addition of water. **(b)** The phase diagrams of LCST and UCST hydrogels, showing the sol-gel transition between the fields. **(c)** Intrinsic responsiveness of hydrogels to pH, due to weak and/or strong ionisation of polyelectrolytes at different pH, resulting in differential swelling in solution.

Hydrogels composed of natural biopolymers are especially capable of mimicking the mechanical properties of biological tissues. These biopolymers are also polyelectrolytes, containing permanently ionised functional groups on their chains acting as hydrophilic binding sites for solvent water molecules, ions. If the polymer contains charges of both polarities, referred to as a polyampholyte, these sites can attract each other, permitting native physical cross-linking between chains, by ionic attractions, hydrogen bonding or physical entanglement. These polymers are highly water-soluble and incorporate water molecules into their 3D structures resulting in swelling and formation of a stable solid-like polymer network. For example, in gelatin, hydrogen bonding shifts the random conformation to a structured one in which single helices associate into triple helices, bringing about the sol-gel transformation [10]. Other natural polymers with similar physical crosslinking mechanisms include agarose, alginate, chitosan, collagen, heparin, hyaluronan, fibrin and matrigel, all of which are entirely natural in origin. Synthetic hydrogels have been developed to address concerns about the durability of these materials, which use man-made polymers lacking ionisation, instead enacting their phase transition by chemical crosslinking, such as by amidation, transesterification or photocatalytic

bond formation by ultraviolet radiation, as exploited by their usage as bioinks in light projection bioprinting. The most common synthetic hydrogels are based on polyethylene glycol and its diacrylate (PEGDA), modified cellulose, methacrylated gelatin (GelMA) and proprietary poloxamers such as Pluronic F-127. These are widely used when control of the rate of natural degradation is necessary, such as in tissue engineering applications, where the rate of proliferation of the host cells must closely match the rate of *in vivo* biodegradation of the matrix while retaining its mechanical stability.

Natural hydrogels can be divided into two subclasses depending on the temperature dependence of their solubility. Those in which cooling from high temperature promotes crosslinking, forming solid gels at room temperature, are classed as being ‘lower critical solution temperature’ (LCST) hydrogels, and those with the opposite behaviour have an ‘upper critical solution temperature’ (UCST), as shown in Figure 1(b). These phase transitions occur on account of thermodynamics, due to the free energy minimisation and polymer-solvent interactions as predicted by the Flory-Huggins solution theory of polymeric colloids, where the curves shown may represent either the binodal (stable coexistence) or spinodal (metastable) phase boundaries. Whether a particular polymer forms an LCST or UCST hydrogel depends on its chemical makeup, which are tunable for synthetic hydrogels, and has great importance for their use in bioprinting, where the nozzle and stage temperatures must be set appropriately for solidification on equilibration to ambient conditions.

Natural protein-based hydrogels can also have their solubility modified by addition of simple salts to the water solution. While the precise mechanism is not fully clear, it is generally observed that ‘kosmotropic’ ions - those that promote the structuring of water through its hydrogen bonding network - result in decreased polymer solubility, such as by citrate, phosphate and tartrate salts. Conversely, the ‘chaotropic’ ions promote disorder and tend to homogenise the phases, increasing solubility, such as by potassium, ammonium and guanidinium salts. These phenomena are widely exploited in various standard molecular biology assays where they result in ‘salting out’ or ‘salting in’ of target proteins respectively. The mechanical (as well as electrical transport) properties of the resulting natural hydrogel can be tuned in this way, where addition of kosmotropic anions during gel formation results in increased hydrogel stiffness due to promoted polymer agglomeration. pH-sensitive crosslinking results in intrinsically responsive hydrogels (Figure 1(c)), a type of functionalised hydrogel, which has inspired numerous innovative new approaches to synthesise composite materials of hydrogels to respond to other stimuli such as light, electricity and magnetism. The latter is the primary focus of this project, where the hydrogel is used as a soft substrate which is actuated by a magnetic matrix interwoven with the hydrogel.

Magnetic Materials

Many traditional actuator applications rely on magnetism to move parts of devices, such as the simple electromagnetic relay switch, but these man-made systems are highly unsuitable for use

in biocompatible applications, and indeed many of the metallic alloys used in modern industrial magnets are toxic in contact with organic tissue.

A potential point of terminology-based confusion originates from the term ‘soft’, which herein refers to the mechanically compliant nature of the hydrogel-based composites, but in the study of magnetic materials has its own meaning, namely, the class of magnetic materials that cannot sustain an internal magnetisation \mathbf{M} in the absence of an external magnetic field \mathbf{B} . Permanent magnetic materials are known conversely as ‘hard’ magnetic materials, develop magnetic fields as a direct result of a quantum mechanical interaction in which unpaired electron spins and electrons in orbitals with net angular momentum spontaneously align to minimise the exchange energy in microscopic regions known as magnetic domains, and are the type of ferromagnets most relevant to this project. There are only three elements on the periodic table which are hard ferromagnets at standard conditions, namely iron, cobalt and nickel, as well as some of the rare-earth lanthanide elements often used for magnetic alloys. Unfortunately, cobalt and nickel are considerably toxic and easily oxidised, limiting their use as biocompatible magnets. Some of iron’s natural mineral forms, magnetite (Fe_3O_4) and maghaemite ($\gamma\text{-Fe}_2\text{O}_3$), inherit iron’s magnetism while being biocompatible, and have given rise to a ‘superparamagnetic iron oxide nanoparticles’ (SPIONs), in which each nanoparticle is fully magnetised to saturation in its own domain, used in medical imaging, tumour treatment and targeted drug delivery. Alterations to the surface chemistry of these particles allows further functionalisation such as in magnetic nanobiocatalysts for protein isolation in affinity chromatography. These magnetic particles retain permanent magnetisation and are a good choice for composite polymeric materials, where the iron oxide nanocrystals are present as precipitate inclusions embedded in the polymer microstructure.

Fibre Spinning

For the applications relevant to this project, bulk composite materials are not the optimal choice of geometry to satisfy the delicate mechanical constraints in operation. Fibrous materials have a higher strength-to-weight ratio than for bulk materials and numerous methods have been developed to fabricate fibres of varying thickness and dimensional tolerances. Traditional methods of fibre spinning include processing the polymer from the molten state, which is useful for thermoplastics but the elevated temperatures can result in degradation in more fragile polymers, especially those relevant to functional micron-scale fibres. Instead, the polymer may be prepared in a suitable solvent, sometimes known as a ‘dope’, which solubilises the polymer and allows extrusion in the monophasic liquid state without the need for heating. Examples of such ‘solution spinning’ techniques include dry spinning, wet spinning, gel spinning and electrospinning.

Electrospinning is a useful electrohydrodynamic technique used to produce submicron diameter polymeric nanofibres within the wider range of electrospraying techniques, which has also found extensive application in nanoparticle synthesis. Under a high voltage, liquid droplets become

charged and elongate through a spinneret due to electrostatic repulsion, breaking surface tension and forming a Taylor cone which permits a fine continuous flow, solidifying in flight to form wound fibres. A modification to use two coaxial flows of liquid before emission allows synthesis of more complex compositions such as two-phase shell-and-tube structures.

A simpler method without the need for high voltage electronics is the dry spinning method, in which a background airflow is enough to evaporate the solvent bound to the polymer fibres. The dry spinning method is most suitable for high-vapour pressure polymer solutions, and is known to favour skin-core fibre morphologies as trapped solvent effuses from the interior of the fibres through micropores [11].

3D Printing of Soft Materials

3D printing is a well-established, democratic (open source) and flexible additive manufacturing method for polymer-based materials, and is a popular alternative to traditional injection moulding well suited for extrusion exploiting the tunable and stimulus-triggered cross-linking of hydrogels. A more specialised extension includes so-called 4D printing, where the time-dependent response of the hydrogel to environmental stimuli can lead to pre-planned folding and migration patterns. For applications involving cell cultures, the soft material (a ‘bioink’) may contain live cells in a hydrogel-biomolecule formulation, either as the fully-formed scaffold, or its precursors (controlled induced cross-linking). One of the principal applications utilising these technologies that is most relevant to the potential extensions of this project is regenerative medicine, an emerging field in biomedical science that widely incorporates 3D printing of soft materials, involving the *in vivo* formation of personalised tissues such as skin, bone and organ tissue. To match physiological environmental conditions the hydrogel may be prepared with phosphate-buffered saline (PBS) instead of deionised (DI) water as the swelling medium. In order to successfully integrate with the host tissue, implanted tissues must contain a matrix (a 3D polymeric scaffold structure mimicking the natural extracellular matrix), signalling molecules (biomolecules such as growth factors and Yamanaka factors to signal stem cell reversion to the pluripotent state) and live cells, depending on the type of tissue to be regenerated. An alternative cell-free approach to tissue engineering involves removing cells from the formulation, and instead using ‘homing’ of host cells into the new scaffold, promoted by the biomolecules. 3D printing of such materials requires a robust deposition method to handle the highly complex formulation properties, with dedicated bioprinters being developed to address these demands. Bioprinting can be done by various methods, adapted from and inspired by the approaches in conventional 3D printing:

- Extrusion: continuous deposition of a viscous bioink stream from a syringe.
- Inkjet: directed emission of bioink droplets from a piezoelectric nozzle.
- Projection: UV-radiation-initiated cross-linking of photosensitive hydrogels

The rheological properties of the bioink (gelation kinetics, surface tension, viscoelasticity, shear-dependent and time-dependent viscosity) are important design parameters, depending on

the printing method. The addition of cross-linkers into the bioink allows the solidification of the hydrogel in the scaffold once deposited. Depending on whether the hydrogel is UCST or LCST, either the syringe or stage must be heated to form the gel before deposition, or, in a recent modification, the freezing of the stage in ‘3D cryoprinting’, to be thawed into the swelled solid state once printing is complete. The cells can be supported on microcarriers suspended in the bioink, which are made of either natural (cellulose, gelatin, collagen) or synthetic (e.g. dextran, plastic, glass) hard materials. This arrangement permits high cell counts to be used without compromising viability, as well as improved nutrient exchange. Some types of cell e.g. chondrocytes can help to replace the scaffold with new ECM tissue if rigidity is desired. Functional materials (e.g. graphene, magnetic fibres, metal nanoparticles) can also be supplied in the bioink with careful control of suspension rheology, orientation and biocompatibility.

Literature Review: Recent Progress in Printable Magnetic Fibre-Hydrogel Composites

The composite systems developed in this project were informed by successful multi-material systems found in the literature as well as those known to be compatible with the equipment available in the Nanoscience Centre at University of Cambridge.

It is only in the past few years that soft multi-material composites of magnetic materials have been conceptualised and appreciated for their scope of applications. Recent advances in multimaterial fibre processing techniques have been enabling the integration of multiple advanced functionalities into individual fibres and textiles. A comprehensive 2020 review [14] describes the wide range of materials compatible with magnetic fibres, outlines a mathematical theory of their material properties and discusses the combination with hydrogels and use with live cells as a highly relevant application. In [13], highly flexible 300 μm diameter soft fibres with up to 1000% breaking strain were developed using the thermal drawing process, with 2-5 μm NdFeCoB microparticles as the magnetic phase and three different soft thermoplastic elastomers, two of which were based on copolymers of polystyrene, as well as a crosslinked silicone filler. These materials are especially relevant to biomedical textiles, as discussed within. In [12], 500 μm diameter SmCo₅ fibres were produced by mixing with polystyrene in toluene, showing a peak tensile strength of 450 MPa. The use of lanthanide alloys likely makes this composition too expensive for widespread use in smart textiles, but illustrates the feasibility of wet-spinning strongly ferromagnetic materials into flexible yet resilient fibres through the use of a polymeric filling, one of the main design goals of this project.

An alternative perspective on the uses of magnetic fibres is provided in [23], where a coil of conductive wire is wound around the straight magnetic fibres to form a self-powered composite, in which axial stretching of the fibre core generates an EMF in the surrounding wire due to Lenz’s law and changes in flux linkage due to area contraction on account of the Poisson’s ratio of the fibre. This field of application has been termed ‘fibertronics’, in which a network of devices employing functional fibrous materials forms a ‘fibre of things’ (FoT), which is one of

the recent specialisations of Dr Huang's biointerface research group at the Cambridge Nanoscience Centre [24].

As is most relevant to the particular scope of this project, 3D printing technology has also been adapted for the partial or total synthesis of fibrous composites [25]. Gelatin-alginate hydrogels have been widely explored for 3D bioprinting of *in vitro* cell cultures as described in a 2021 review [26], which was used to inform the selection of such a hydrogel in this work. In these materials, the natural peptide biopolymer gelatin provides the rapid temperature-dependent UCST gelation kinetics, while the polysaccharide copolymer alginate, with its tunable proportion of G-blocks (α -L-guluronate) and M-blocks (β -D-mannuronate), serves as a passive structural support while maintaining biocompatibility [29]. The G-blocks in the alginate biopolymer can also be ionically crosslinked with Ca^{2+} ions providing another method of varying the rheological properties of the system [27]. 3D printing of gelatin-alginate hydrogels can easily mimic complex biomimetic tissues to high geometric tolerances [28], and 3D bioprinters designed to handle variable viscosity solutions can be equipped with the nanospinning extrusion techniques, such as Printer.HM [22], to synthesise 3D multi-material functional hydrogel composites to a wide variety of specifications.

2.2. Project Scope

Initial Goals and Context

The modular nature of this project - for the synthesis of the fibres, the hydrogels and the composites - made for a straightforward, mostly linear roadmap throughout the year. However, the overall progress made on the project has been a little less than forecasted at the beginning of the year. It was intended to spend Michaelmas term on the fibres, Lent term on the hydrogel and adding it to the fibres to form the composite, and then finally Easter on utilising the Nanoscience Centre bioprinter 'Printer.HM' to print the system with a seeding of epithelial cell culture as the end goal, as a prototypical substrate for an *in vitro* lung organoid. The method of applying the magnetic forces was left open at the time, with early attempts with bar magnets falling short.

Revised Project Goals

While the investigation of hydrogel-fibre composites were completed and tested in their entirety, a suboptimal rate of working throughout Michaelmas led to the decision during the Lent mid-term review to abandon the integration with live cells (and therefore removing the need to use the bioprinter), leaving them to discussion in this report only. Based on feedback from the Technical Milestone Report submitted at the start of Lent term, more emphasis was placed on obtaining quantitative data to make up for the absence of novel experimentation in the Easter term due to the shift in goals. The main product of this project is therefore the fibre-hydrogel composite, which has been produced using techniques that, with minimal further research, could be integrated with a 3D bioprinter and cell culture, as discussed in Section 6.2 of this report.

③ Theory and Experimental Design

3.1. Theoretical Treatment

In this project, the magnetic fibres are modelled as elastic beams constrained at their ends to represent the overhanging and underhanging sections spun around the frame. The fibres are subject to their own self-weight and a magnetic force in the transverse direction hanging in a compliant hydrogel medium.

Structural Mechanics

A simplistic analysis of the setup used to test the fibre composites is initially performed using static Euler-Bernoulli beam theory. In this model, the stiffness of the hydrogel is presumed to be sufficiently low to not resist the deflections of the fibre, and the resultant deflection of the hydrogel is decoupled from the fibre. Due to adhesion of the fibre to the surface of the horizontally-oriented frame at each end, the fibres are effectively clamped at each end, as depicted in Figure 2 (although it is noted that this assumption breaks down when the fibres are manually contracted in length due to their slackening). This system is now a linear superposition of a statically indeterminate beam and a uniformly distributed load (UDL) which can be solved for the shear forces $S(x)$, bending moments $M(x)$ and transverse displacements $y(x)$ by equilibrium with the load per unit length $w(x)$ and compatibility $dy/dx = 0$ at $x = -l/2$ and $x = l/2$.

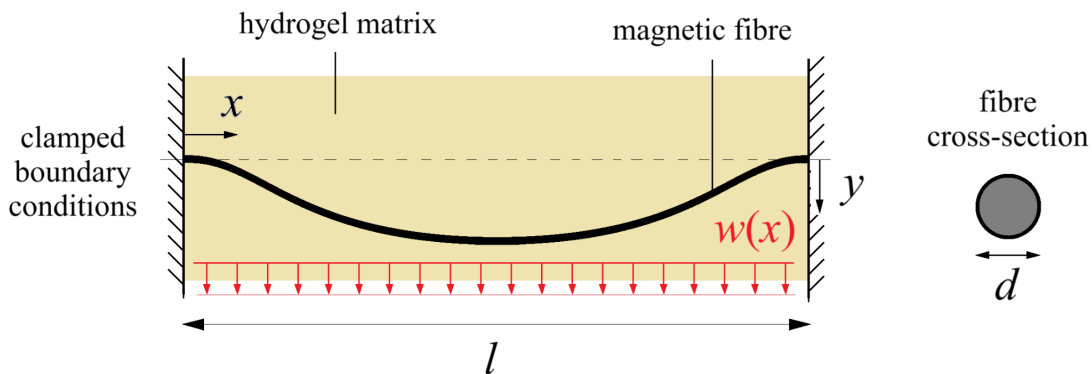


Fig. 2. Diagram of the magnetic fibre modelled as a structurally elastic element clamped between two supports separated by a distance l . The shape of the displaced fibre $y(x)$ is illustrated. A simple solid circular cross-section of a fibre is shown with diameter d .

For fibres spun to a length l between supports, with no contraction, with Young's modulus E , second moment of area I (flexural rigidity EI), the clamping moments at the ends of the fibre are

$$M(-l/2) = M(l/2) = \frac{wl^4}{12} \quad (\text{Equation 1})$$

To determine expressions for $S(x)$, $M(x)$ and $y(x)$, we consider a linear superposition starting with a statically determinate simply-supported beam under a UDL $w(x)$, apply the necessary moment to enforce compatibility with zero angle at the ends and solve the equilibrium equation. The resulting expressions of this analysis are:

$$S(x) = \frac{dM}{dx} = wx \quad (\text{Equation 2.1})$$

$$M(x) = -EI \frac{d^2y}{dx^2} = \frac{w}{2} \left(x^2 - \frac{L^2}{12} \right) \quad (\text{Equation 2.2})$$

$$y(x) = \frac{w}{384EI} (8L^2x^2 - 16x^4 - L^4) \quad (\text{Equation 2.3})$$

From this, it is observed that the bending moment in the fibre does not exceed the clamping moments, and the maximum displacement can be found:

$$M_{max} = \frac{wl^4}{12} \text{ at } x = \pm \frac{l}{2} \quad \text{and} \quad y_{max} = \frac{wl^4}{384EI} \text{ at } x = 0 \quad (\text{Equation 3})$$

The intended applications of these magnetic fibres will be expected to involve cyclic loading of the magnetic field, hence making fast fracture due to fatigue a critical failure mode of the fibres, occurring at lower stresses than at plastic yield. It is commonly accepted that the maximum high-cycle fatigue design stress, for infinite cycles to failure, for many materials is approximately half of the yield strength σ_y , which places an upper bound on the maximum load w from Equation 3. If the second moment of area for the circular cross-section is $I = \pi d^4/64$, the maximum allowable stress $\sigma_y/2$ then applying $\sigma = My/I$ gives an upper bound on the allowable magnetic force per unit length to prevent fatigue-induced failure:

$$\frac{16wl^2}{3\pi d^3} \leq \sigma_y \quad \Rightarrow \quad w \leq \frac{3\pi}{16} \frac{d^3 \sigma_y}{l^2}. \quad (\text{Equation 4})$$

Hydrogel Deformation

With an estimate of the fibre deflection $y(x)$ in Equation 2.3, the effects of the hydrogel can now be investigated. While a rigorous analysis might involve modelling the hydrogel as a continuum subject to a line of prescribed deformations due to the fibre, a simpler method is to modify the plane strain elastic beam model by incorporating a continuous distributed viscoelastic reaction force across the fibre representing the contact with the hydrogel, based on a Kelvin-Voigt linear viscoelasticity model. At steady state, the viscosity of the hydrogel does not contribute a force, and the equilibrium condition simplifies to the Winkler support model [17], given by:

$$EI \frac{\partial^4 y}{\partial x^4} + \eta \frac{\partial y}{\partial t} + ky(x, t) = w(x, t) \quad \xrightarrow[\dot{y} = 0]{\text{steady-state}} \quad EI \frac{\partial^4 y}{\partial x^4} + ky = w \quad (\text{Equation 5})$$

where k is the stiffness of the hydrogel per unit length. Equation 5 was solved using Python's `scipy.integrate.solve_bvp` function in terms of the characteristic reciprocal length $\lambda_w = \sqrt{\frac{k}{4EI}}$, so that $\frac{d^4y}{dx^4} + 4\lambda_w^4 y = \frac{w}{EI}$ with boundary conditions $y(\pm\frac{l}{2}) = 0$ and $\frac{dy}{dx}(\pm\frac{l}{2}) = 0$.

This allows us to examine the effect of the stiffness-to-rigidity ratio k / EI on the maximum displacement, where the model reduces to Equation 2.3 in the case of $k = 0$ (no hydrogel).

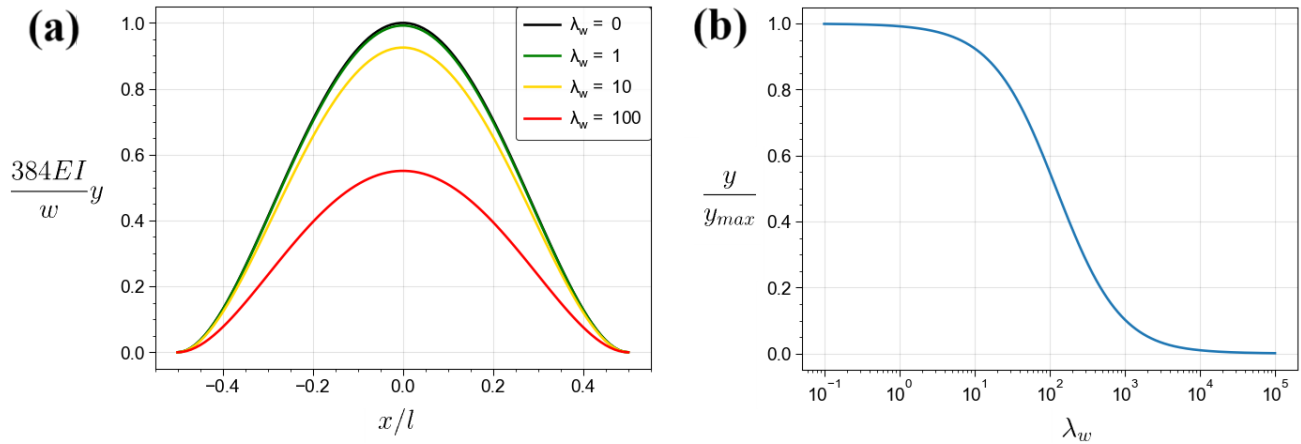


Fig. 3. (a) Displacement $y(x)$ of a magnetic fibre based on Equation 5 for a variety of hydrogel-to-fibre stiffness ratios (dimensions of λ_w : L^{-1}) illustrated with $w = 1$, $EI = 1$ and $l = 1$. The ‘no hydrogel’ case is marked in black. **(b)** Knockdown factor in peak displacement at $x = 0$ for a wide range of λ_w , showing little impact for $\lambda_w < 10$, and immobilising the fibre for $\lambda_w > 1000$.

Magnetic Force

We now need to estimate the magnetic force loading. A finite element of a hard ferromagnetic material possessing internal magnetisation \mathbf{M} , exposed to an external magnetic field of flux density \mathbf{B} , experiences a resultant force \mathbf{F} and torque $\boldsymbol{\tau}$ per unit volume of material:

$$\mathbf{F} = \nabla(\mathbf{M} \cdot \mathbf{B}) \quad (\text{Equation 6.1})$$

$$\boldsymbol{\tau} = \mathbf{B} \times \mathbf{M}. \quad (\text{Equation 6.2})$$

If the field \mathbf{B} is approximately unidirectional and parallel to \mathbf{M} , and oriented with the North-South axis perpendicular to the fibre (in the z -axis direction), then Equation 6.1 simplifies:

$$\mathbf{F}_{mag} = M_0 \frac{dB_z}{dz} \hat{\mathbf{k}} \quad (\text{Equation 7})$$

where $\mathbf{M} = M_0 \mathbf{k}$ is the magnetisation aligned in the \mathbf{k} -direction (z -axis), and the torque $\boldsymbol{\tau} = \mathbf{0}$ as expected from a soft magnetic material (or a hard magnetic material at equilibrium).

The magnetic field surrounding a solenoid electromagnet can be represented as that surrounding a cylindrical ferromagnet with current-dependent magnetisation M_z . For a solenoid of radius R ,

height L , and magnetomotive force (ampere-turns) NI , this is given by the total magnetic moment per unit volume, $M_z = \pi N I R^2$. By solving the relevant Poisson's equation with a suitable magnetostatic potential, the external \mathbf{B} -field on the magnetisation axis can be found [15]:

$$B_z(z) = \frac{1}{2} M_z \mu_0 \left(\frac{\frac{L}{2} - z}{\sqrt{(\frac{L}{2} - z)^2 + R^2}} + \frac{\frac{L}{2} + z}{\sqrt{(\frac{L}{2} + z)^2 + R^2}} \right) \quad (\text{Equation 8})$$

Differentiating Equation 8 with respect to z and substituting into Equation 7 gives an expression for the magnetic force:

$$F_{mag} = 4\pi NI \mu_0 M_0 R^4 ((L + 2z)^2 + 4R^2)^{-3/2} - ((L - 2z)^2 + 4R^2)^{-3/2} \quad (\text{Equation 9})$$

The force is dependent on the displacement z of the fibre, leading to a complex coupling with no analytical solution. However, if it is presumed that $\Delta y = \Delta z \ll L$, then these second-order effects can be neglected and an approximate solution can be obtained. The graph of the semi-normalised force $-F_{mag}/NI\mu_0 M_0$ (dimensions: \mathbf{L}) against z/L for different aspect ratios R/L with a basis of $L = 1$ is shown in Figure 4, where it is observed that there is generally a peak in F_{mag} at some distance $z > L/2$ from the centre of the magnet, representing a small distance away from the electromagnet surface. A magnetic fibre placed here would, assuming constant M_0 , experience the maximum possible force. It is also found that short and stubby electromagnets (larger R/L) produce higher maximum forces at this optimal distance.

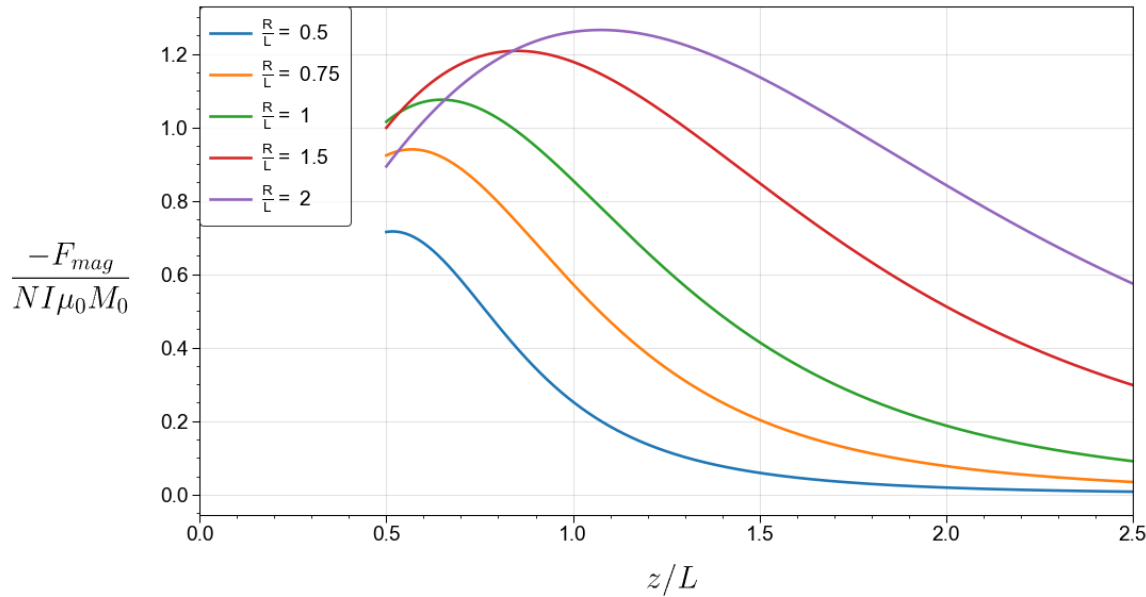


Fig. 4. Plot of force on a magnetic fibre at distance z from the centre of an electromagnet with radius R and length L , using Equation 9, for different ratios R/L with $L = 1$.

The position $z/L = 0.5$ represents the end surface of the electromagnet.

To obtain an estimate of M_0 , we require the magnetic properties of the fibres. Referring to the B - H characteristic curve for Fe_3O_4 nanoparticles in poly(styrene-divinylbenzene) matrix obtained in [16], a saturation magnetisation of approximately $80 \text{ A m}^2 \text{ kg}^{-1}$ (per kilogram of Fe_3O_4) is easily attained in the fibre for applied fields above $H > 500 \text{ A/m}$ (corresponding to $B > 670 \mu\text{T}$). Lower bound estimates based on Equation 8 produce fields within the range necessary to achieve saturation for all feasible distances ($\frac{1}{2} < \frac{z}{L} < 1$), so the assumption of constant M_0 (per unit concentration of iron) is deemed appropriate.

Composite Properties

Based on a simple rule of mixtures, lower and upper bounds can be established for the modulus and yield stress of an anisotropic composite, corresponding to the extreme cases of parallel and perpendicular fibres. This technique can be applied both to the hydrogel-fibre composite as well as the fibre itself. The moduli E and yield strength σ_y of the matrix (subscript m) and fibres (subscript f , fracture strength $\sigma_y^{(f)}$) in terms of the volume fraction of fibres V_f by

$$\underbrace{\left(\frac{V_f}{E_f} + \frac{1 - V_f}{E_m} \right)^{-1}}_{\text{modulus transverse to fibres}} \leq E \leq \underbrace{V_f E_f + (1 - V_f) E_m}_{\text{modulus parallel to fibres}} \quad (\text{Equation 10.1})$$

$$\sigma_{ts} = V_f \sigma_y^{(f)} + (1 - V_f) \sigma_y^{(m)} \quad (\text{Equation 10.2})$$

Since the hydrogel-fibre composite is to be actuated transverse to the fibres, it is appropriate to take the lower bound of Equation 10.1 for its effective modulus. Since this expression is a harmonic mean of the component moduli weighted by volume fractions, the most compliant component dominates, and so the composite modulus can be considered equal to that of the hydrogel ($E \ll 1 \text{ MPa}$). A naive estimate for the fibre modulus could use the upper bound, expressing in terms of mass fractions m_f and densities (Equation 11.1), but in reality the complex amorphous fibre requires experimental testing, which was not performed in this project. In the literature [20], up to a 300% increase in Young's modulus and 60% increase in tensile strength is known in polypropylene fibres when combined with 20 wt% iron oxide microparticles of diameter less than 33 μm , highlighting the high sensitivity to the presence of these magnetic materials.

$$E_{\text{composite}}^{(\perp)} = \left(\frac{V_f}{\frac{m_p}{\rho_p} E_p + \left(1 - \frac{m_p}{\rho_p}\right) E_m} + \frac{1 - V_f}{E_{\text{hydrogel}}} \right)^{-1} \quad (\text{Equation 11.1})$$

$$\sigma_{ts,\text{composite}}^{(\perp)} = V_f (V_p \sigma_y^{(p)} + (1 - V_p) \sigma_y^{(m)}) + (1 - V_f) \sigma_y^{(\text{hydrogel})} \quad (\text{Equation 11.2})$$

Since $E_{\text{hydrogel}} \ll E_m, E_p$, then $E^{(\perp)}_{\text{composite}} \approx E_{\text{hydrogel}}$, and the composite strength is a sum of weighted contributions from the polymer (p), magnetic material (m) and hydrogel.

Material Selection

Based on the literature review and advice from my supervisor, a shortlist of candidate materials serving the purpose of fibre spinning solvent, fibre filler polymer, fibre magnetic material and hydrogel matrix was prepared:

Fibres			Hydrogels
Spinning solvents	Filling polymers	Magnetic materials	
N,N -dimethylformamide (DMF)	poly(ethylene oxide) (PEO)	iron(II, III) oxide (Fe_3O_4)	gelatin
acetone	polystyrene (PS)	neodymium alloy ($\text{Nd}_2\text{Fe}_{14}\text{B}$)	sodium alginate
methyl ethyl ketone (MEK)	polyurethane (PU) poly(3,4-ethylenedioxy thiophene) polystyrene sulfonate (PEDOT:PSS) platinum-cured silicone (EcoFlex 00-10)	samarium-cobalt alloy (SmCo_5)	

Table 1. Materials considered for the synthesis of the magnetic fibre composite.

Considering that the purpose of the fibre composite is to attain deflections with high sensitivity to the magnetic field without yielding, this can be stated as a stiffness-limited design problem with an additional component accounting for magnetisation. In terms of the purely mechanical properties, we aim to maximise the performance index σ_y^2 / E (σ_y : yield stress, E : Young's modulus). A preliminary inspection of the CUED Materials Databook showed that polymers and materials based on natural materials are optimal for this design criterion. Ansys Granta EduPack (ver. 2022 R2) was then used to conduct a wider search across the Level 3 Database of materials, summarised in the materials property chart in Figure 5, allowing a closer inspection of the feasible materials used to construct the fibres. The green dashed line has gradient 2 on the log-log axes, representing the contours of the performance index function, maximised below the line. The magnetic materials are typically non-technical ceramics (e.g. iron oxide) or metals (e.g. SmCo_5). The bubbles for 'elastomers' (light blue), 'natural fibres' (light brown) and 'fibres and particulates' (grey/black) contain the maximum values of this performance index, indicating their optimality in this material selection task.

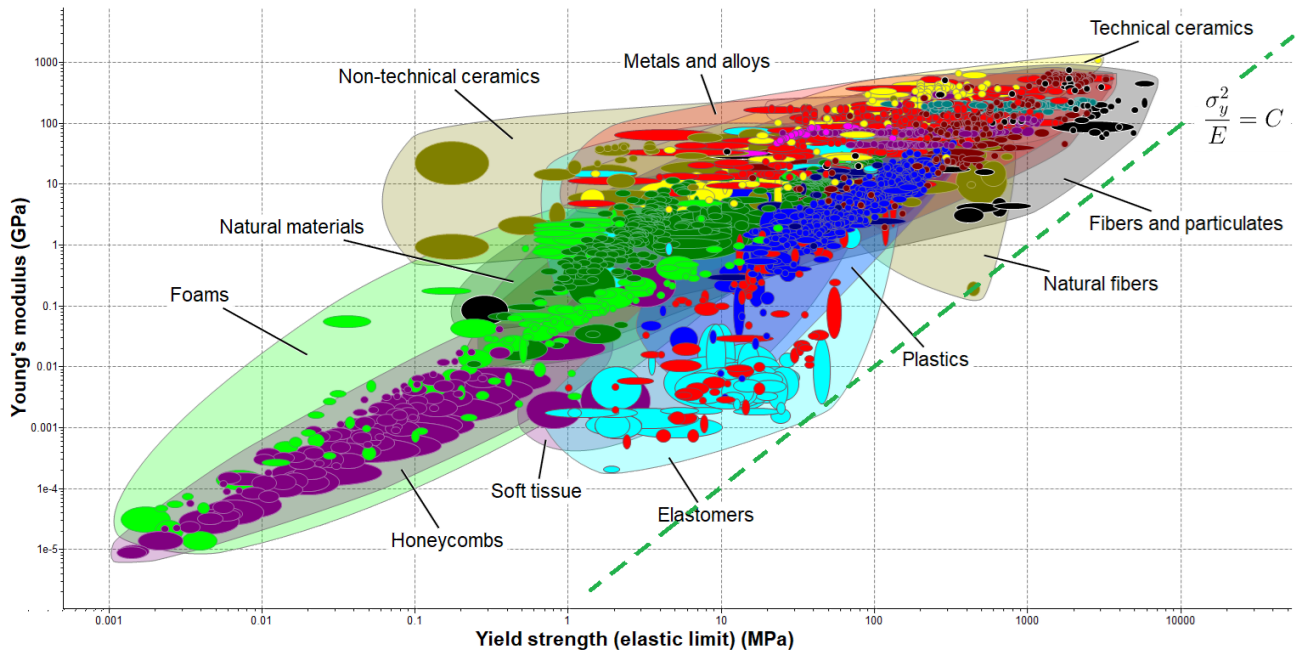


Fig. 5. Material property chart of yield strength σ_y [MPa] against Young's modulus E [GPa] for a wide range of materials, obtained from the Level 3 Database in Ansys Granta EduPack.

Computational Modelling (Finite Element Analysis)

The theory discussed thus far is only intended as a rough approximation, and the inherently large fabrication variability of the constituent materials limits precise predictions of experimental observations, and are instead intended as tests for feasibility of such a magnetic hydrogel composite construction. A more robust (but still imperfect) method is the use of computational modelling. In this project, the CAD software SOLIDWORKS (ver. 2022) was applied extensively to prepare models of the hardware used in the experiments, and also as structural mechanics solver using the ‘Static Study’ tool under the ‘Simulation’ tab in SOLIDWORKS. Using a representative fibre diameter of $d = 15 \mu\text{m}$, with each fibre as a single closed loop around the frame for modelling simplicity, the schematic in Figure 6 was created. Due to the unnecessary computational complexity of modelling all fibres, this model is only presented for graphical illustration and a reduced model is used to carry out simulation studies. Detailed dimensioning information for the frame can be found in Section 4.1, and the object under study is shown in Figure 7. The assembly shown in Figure 7 is comprised of three parts (supports, fibre, hydrogel) with suitable contact and parallel separation mates applied.

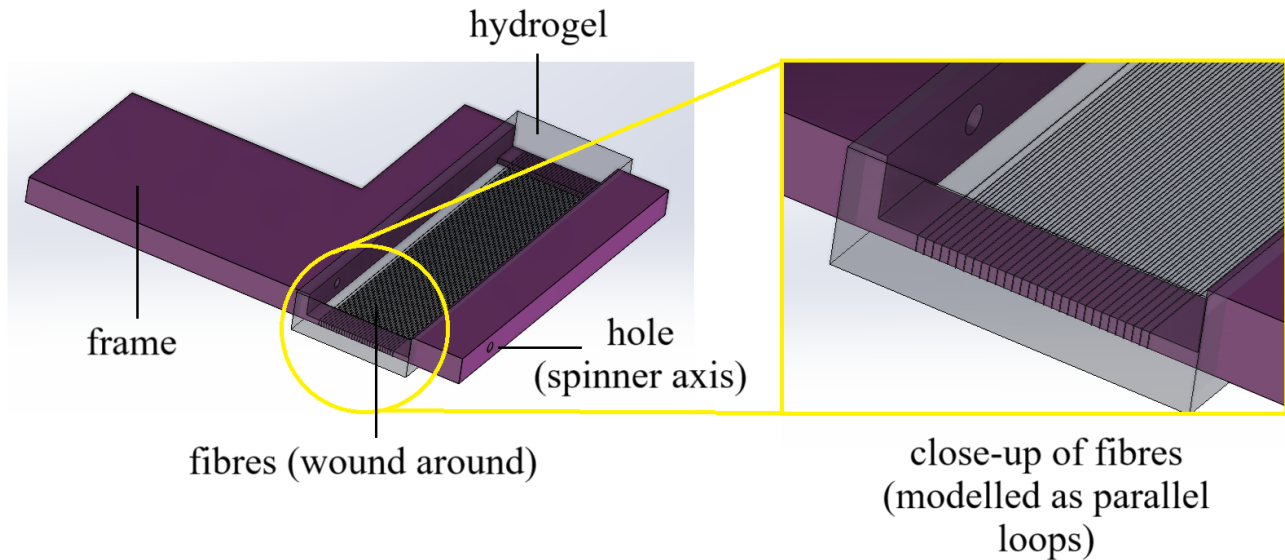


Fig. 6. SOLIDWORKS model of the fibres on the frame. Using a linear pattern, 30 parallel loops representing fibres (black) were placed on the frame (purple), each of diameter $\varnothing 15 \mu\text{m}$, covering a distance along the frame of 6 mm (separation 0.2 mm). The end-to-end length of each fibre section is 28 mm. The hydrogel (clear, grey) is represented as a cuboid covering the fibres and frame completely and extending above and below by an additional 0.5 mm.

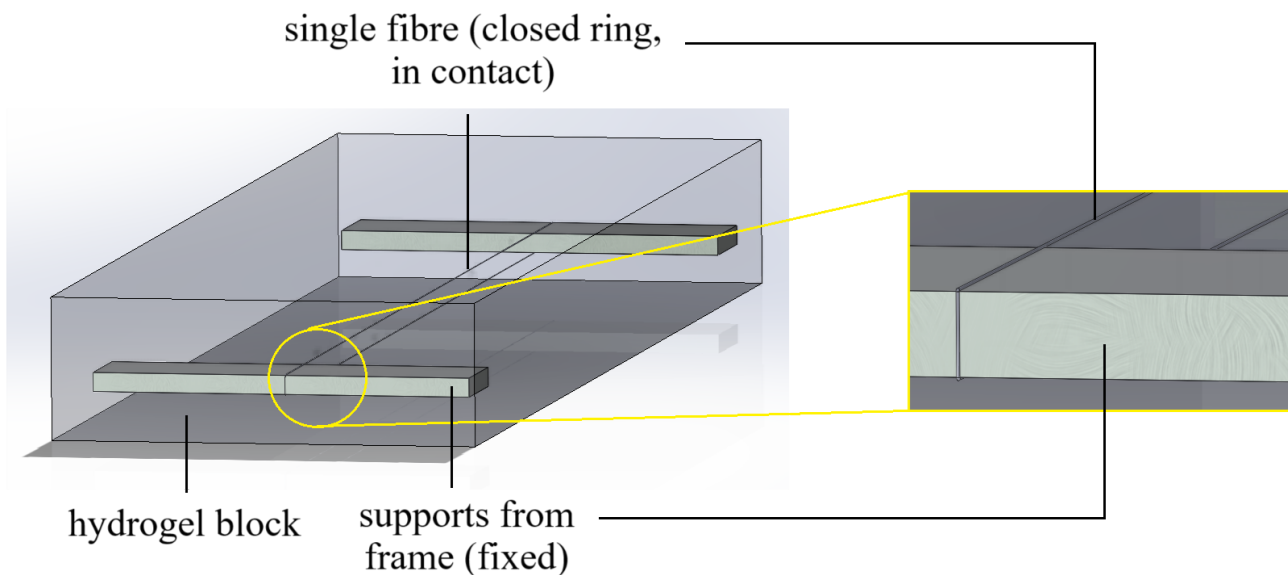


Fig. 7. SOLIDWORKS model of a single closed loop representing a fibre (diameter $\varnothing 15 \mu\text{m}$), a horizontal distance of 28 mm across. The support cross-section is $0.4 \text{ mm} \times 2.0 \text{ mm}$.

In the SOLIDWORKS static study, material properties were assigned to each part. The hydrogel provides the largest source of uncertainty since its properties are highly variable, and information in the literature is generally scarce for any particular composition of hydrogel, so the Young's modulus E was deduced using nonlinear least-squares from the 'Table 1' in [18] to estimate a 6%

gelatin, 1% alginate hydrogel as used in practice for one of the experiments, finding $E = 570$ kPa as a reasonable value. The model estimation is described in Appendix II. The Poisson's ratio was assumed to be 0.49 (almost fully incompressible, typical for rubbery substances) and the shear modulus was computed using $G = E / (2(1 + \nu))$. The tensile strength was estimated from a 4% gelatin hydrogel in 10 mM NaCl in [19], likely with large variation. Two UDLs of 1 mN total force were applied vertically to each lengthwise fibre section, and a custom high-quality mesh with minimum element size 0.009 mm was generated to properly capture the morphology of the micron-scale fibres. The simulation was run with the 'large displacements' flag, taking 15 minutes to solve completely consuming a peak of 4 GB of RAM. The resulting deformed structure is shown in Figure 8, with a maximum displacement of 0.688 mm.

Part	Material	Mechanical properties				
		ρ [kg m ⁻³]	E [Pa]	G [Pa]	ν [-]	σ_y [Pa]
supports	Alloy Steel	7700	2.1×10^{11}	7.9×10^{10}	0.28	6.204×10^8
fibre	PS Medium/High Flow	1040	2.28×10^9	8.173×10^8	0.387	3.59×10^7
hydrogel	[custom material]	1000	5.7×10^5	1.9×10^5	0.49	4290

Table 2. Material properties assigned to each part in SOLIDWORKS.

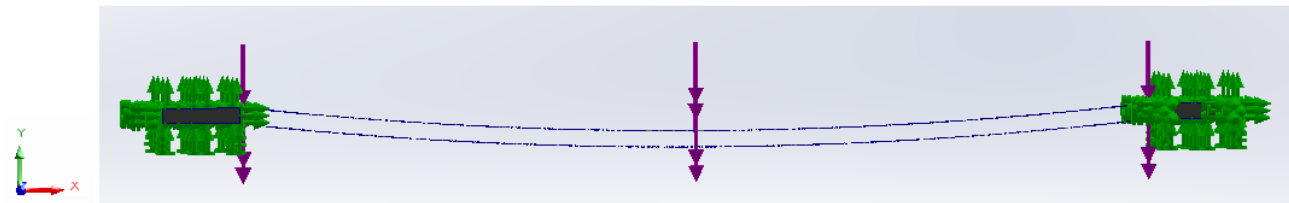


Fig. 8. Displaced structure under a 1 mN load. The hydrogel is hidden from view since its displacement was negligible. A central displacement of 0.7 mm is found.

Although the SOLIDWORKS study seemed reasonable based on experimental experience, a theoretical estimate based on Equation 3 yielded unrealistically large displacements, suggesting that the applied force perhaps does not reflect the true magnetic forces experienced in practice.

Next, COMSOL Multiphysics (ver. 6.2) was employed in an attempt to more faithfully capture the magnetomechanical interactions of the model. The SOLIDWORKS assembly was split into quarters at plane cuts, exploiting symmetry to reduce computational complexity, saved as a Parasolid file (.x_t) and imported into COMSOL to form the geometry, and a quarter-cylindrical geometry was also created to represent the electromagnet. A 3D multiphysics 'Stationary' study utilising the 'Magnetomechanics, No Currents' interface was prepared. Magnetic flux conservation was enforced in the magnetised domains and materials properties were assigned. Unfortunately due to lack of expertise with the COMSOL software I encountered an error when computing the stress and strain variables which I was unable to resolve, but the

magnetic field due to the electromagnet was found successfully, shown in Figure 9. The error returned from COMSOL was as follows:

Spatial Mesh Displacement

Undefined value found.

- Detail: Undefined value found in the equation residual vector.

There are 10 degrees of freedom giving NaN/Inf in the vector for the variable comp1.spatial.u.

at coordinates: (0,0,-0.00195), (0,5.01891e-05,-0.00195), (0,0.000100378,-0.00195), (5e-05,0,-0.002), (3.53553e-05,5.01891e-05,-0.00196464), ...

This appears to be due to erroneous boundary conditions when setting up the model but lack of time and familiarity with the software combined made this infeasible to debug at the time.

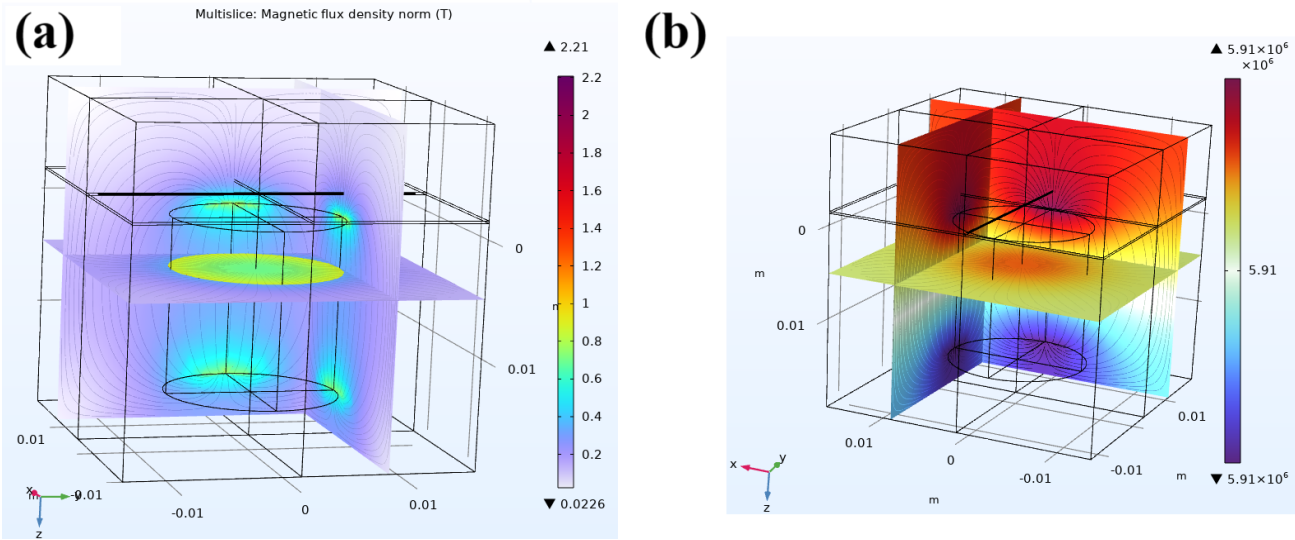


Fig. 9. (a) Magnetic flux density \mathbf{B} , showing magnitude (as colourbar, in Tesla) and field lines on the planes $x = 0.075$ and $y = 0.075$. (b) Magnetic scalar potential ψ , such that $\mathbf{H} = -\nabla\psi$. The fibre is visible in the xy plane at a z just above the top side of the cylinder.

The simulation verifies with the assumption of a strong magnetic field just above the poles of the magnet, concentrated in the middle. However, it does show that the assumption of uniformity in the magnetic field across the fibre is likely less accurate than discussed previously, as the field lines curve back around in the fibre regions near the supports. Due to the large uncertainties in material properties, even sophisticated computational studies are challenging to design with any numerically accurate predictive power. For this reason, the emphasis in analysing the mechanical deformations was on experimentation rather than simulation, the latter of which was only used as a rough guide to check orders of magnitude, as well as to feed back into informing material selection.

3.2. Design of Experiment

The nanospinning technique is widely used by Dr Huang's biointerface research group in the Nanoscience Centre and was co-opted for this project under the guidance of my PhD student supervisor Yaqi. However, a key challenge novel to this project was the actuation aspect, in which it was found that spinning the fibres to a fixed length results in fibres that were slightly under tension due to thermal contraction from the warm fibre solution state. This made them resistant to deformation from transverse forces. To overcome this difficulty, variable-length frames were developed in which the fibres could be spun at a particular length, then the distance between the contacts decreased slightly in order to relax the fibres (effectively turning them into structural cables rather than beams in tension), from which actuation was much more sensitive. It was aimed to contract the fibres by such a small distance to just relieve the fibres of their internal tension without causing a noticeable sag when no magnetic forces are active. The details of this procedure are discussed in Section 4.2.

Frame Design

Numerous designs of frames used to spin the fibres were proposed and tested, realised by 3D printing in tough PLA. The millimetre-scale dimensions put additional stability limitations in fabrication from the 3D printer, and some designs were unsuitable due to poor frictional contact between the slider and the frame, which led to needing several iterations of design before a suitable model of frame was found. Figure 10 shows the iterations of design in chronological order, with the final design being model (g). The clearance between the fork and slider was trialled at 0.0 mm, 0.2 mm, 0.4 mm, 0.6 mm, 0.8 mm and 1.0 mm, aiming for a trade-off between defect tolerance and frictional contact, with the best fit being 0.2 mm, so the fork thickness in (g) was 2.0 mm while the slider gap was 2.2 mm.

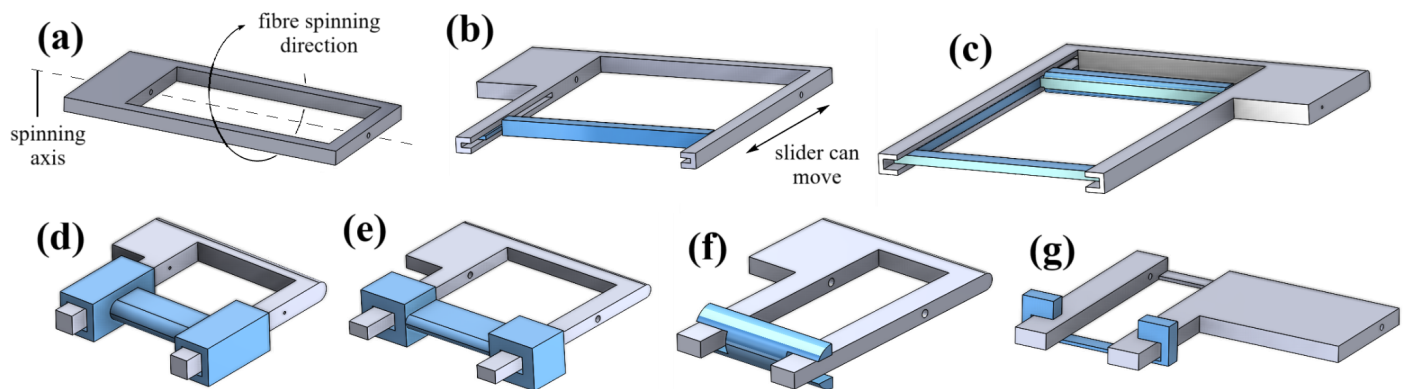


Fig. 10. Evolution of tested variable-length frames, as SOLIDWORKS assembly models, consisting of a fixed frame (shown in silver) and a moving slider (shown in blue) which moves along the forks of the frame to achieve a tunable distance between the fixed support and the variable support. (a) Base design (fixed: no slider). (b) Slider inside forks. (c) Two spinning regions: one fixed length, one variable length. (d) Slider outside forks. (e) Thinner forks and tighter fit. (f) Curved contacts, back to inside. (g) Very thin contacts, slider sits on forks.

④ Materials and Methods

4.1. Apparatus

Spinning Frame

The CAD drawings (in third-angle projection) for the final design of frame and slider is shown in Figure 11. There is an additional clearance of 0.2 mm between the frame fork and the slider.

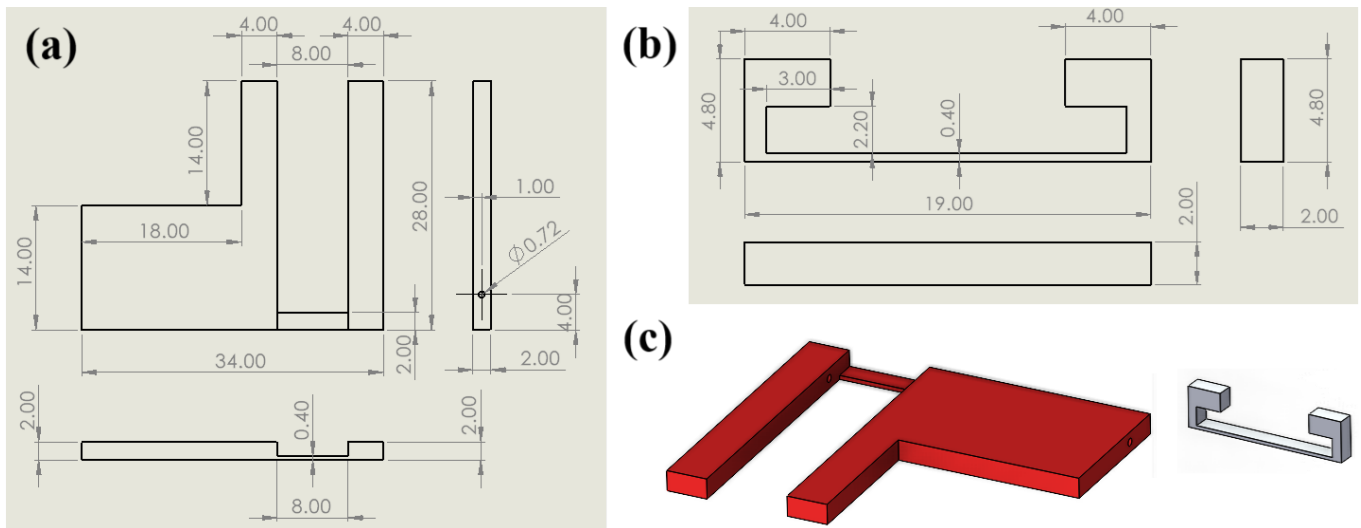


Fig. 11. (a) Drawing of frame. (b) Drawing of slider. (c) Auxiliary views of parts, shaded in colour. Note: the scales of (a) and (b) are **not** equal. Dimensions are indicated in mm.

These frames were made in PLA using the UltiMaker 3D printers available in the Electrical Engineering building. It was found that the precision of the slider could be significantly refined by printing it on its side rather than upright, the latter of which caused sagging of the ends which caused issues in fitting to the frame. To print, the SOLIDWORKS model parts were exported as STL files, generating the triangulated mesh, tuning the printing settings (Table 3) and slicing to produce the printing instruction file (.gcode) which is uploaded to the printer. For better visibility on the camera when taking measurements, the frame was printed in red while the slider was printed in white.

Material	Resolution	Infill density	Infill pattern	Adhesion
PLA	0.15 mm	20%	Triangles	On

Table 3. Printing parameters in UltiMaker Cura.

Chemical Stock

Many of the chemicals were already present in the Nanoscience Centre lab (either Module 1 or the biolab's chemical cabinet). Others were purchased through the department's supplier, Merck (formerly Sigma Aldrich). Table 4 shows a selection of the main chemicals used. Volatile solvents such as DMF and acetone were stored in ventilated safety cabinets while not in use.

Chemical	CAS No.	Information
Iron oxide	1317-61-9	iron(II, III) oxide, powder, < 5 µm, 95%
Polystyrene	9003-53-6	average $M_w \sim 280,000$ by GPC
Gelatin	9000-70-8	from porcine skin, gel strength 300, type A
Sodium alginate	9005-38-3	from <i>Macrocystis pyrifera</i> , M/G ratio ≈ 1.56

Table 4. The four main chemicals used to develop the successful composites in this project.

Electronics

Arduino microcontrollers were used to power a spinner (a stepper motor with a 22 gauge blunt needle tip, outer diameter 0.718 mm, programmed to turn continuously at constant speed) and an electromagnet (sourced from RS Components, programmed to switch 'on' and 'off' every 1.0 seconds. Solderless breadboards were used with 5 V and 9 V power sources down-converted from the mains supply. Analog components were sourced from the ADALP2000 kit. The combined systems are shown schematically in Figure 12.

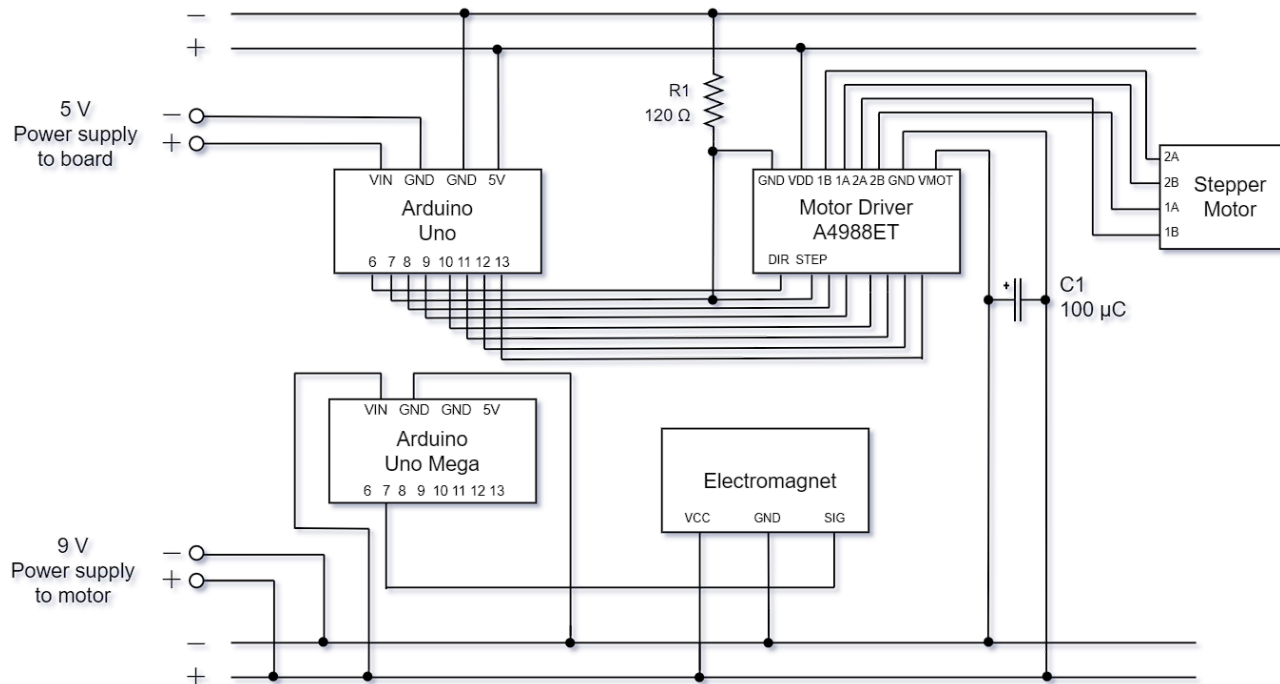


Fig. 12. Circuit schematic for the spinner, using an Arduino-controlled stepper motor.

Software

The programming for the Arduinos was straightforward, with the code for the spinner already loaded onto the Arduino without need for modification, and is available in [22]. The electromagnet was programmed in C++ in the PlatformIO tool in Visual Studio Code. The code is practically identical to the standard `blink.ino` example code.

A robot arm (uArm Swift Pro Standard 4 DoF) was used to control the automatic spinning process. The robot arm was programmed using its Python API (identical to the arm used in Printer.HM [22]), employing multithreading to enable interrupts, connecting via USB serial communications. The source code for the robot arm (during spinning) is in Appendix III. When testing fibre deflections, the same robot arm was used with modified code, with a 3D-printed custom mobile phone holder tool to move the phone's camera to the appropriate position in order to record the deflections of the composite relative to the frame under the magnetic forces.

4.2. Experimental Techniques

Preparing Spinning Solutions

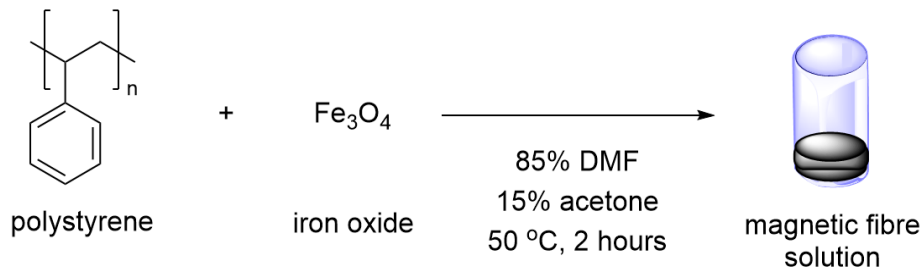


Fig. 13. Scheme for the synthesis of a magnetic fibre solution, using PS as a polymer filler.

The following procedure was used to prepare each fibre solution:

1. Place a clean, dry, small capped glass vial on a balance to measure its dry mass.
2. Working inside a microbiological safety cabinet (MBSC) with a HEPA filter, place down the uncapped glass vial and the solvent containers of DMF and acetone.
3. To the glass vial, add 850 μL of DMF using a precision micropipette; dispose of the tip.
4. To the glass vial, add 150 μL of acetone using the micropipette; cap the vial.
5. Weigh the filled glass vial on the balance and record the mass; calculate the mass of the 1000 μL solvent by difference; place the vial back in the MBSC. Record this as m_0 .
6. Calculate the appropriate masses of polymer and iron oxide necessary to achieve a final composition of 100x wt% polymer and 100y wt% iron oxide using Equation 12:

$$\text{mass of polymer} = \frac{xm_0}{1 - (x + y)}; \quad \text{mass of iron oxide} = \frac{ym_0}{1 - (x + y)} \quad (\text{Equation 12})$$

7. Place a clean plastic weighing boat on the balance; tare (zero) the balance.
8. Using tweezers, pick and place the appropriate mass of polymer beads into the weighing boat, aiming to get as close as possible to the target mass.
9. Using a spatula, carefully weigh out the appropriate mass of iron oxide powder into the weighing boat.
10. In the MSBC, funnel the polymer beads and iron oxide powder into the solvent vial.
11. Drop in a small magnetic stir bar; cap the vial; seal the cap with Parafilm; label the vial with the composition of the solution.
12. Place a blob of Blu-tack on the bottom of the vial and stick the vial to the centre of a hot plate, heating at 50 °C and using the magnetic stirrer at a low power for approximately 2 hours to produce a viscous homogeneous black solution. The solution can be used to spin fibres straight from the heated state, or from cooling (though ideally with a little reheating to ensure full solubility).

Automatic Wet Spinning of Fibres

Once a fibre solution had been prepared, the following procedure was used to prepare a frame holding fibres across its length:

1. Working inside an MSBC, get a frame and slider, produced from the 3D printer; attach the slider on the ends of the ‘fork arms’ of the frame (at full length).
2. Set up the laptop running the uArm spinner Python program (Appendix III) and connect to the uArm robot arm. Turn on the power source for the Arduino-powered spinner. Push the pole of the spinner through the holes in the frame to make it spin on its axis. Using the command line inputs, position the robot arm approximately 5 cm directly above the spinning frame, aligned with the right-hand edge of the frame as accurately as possible.
3. Unseal and uncap the desired fibre solution glass vial, and carefully draw up approximately 1 ml of the solution into an uncapped syringe, and then quickly cap the syringe with a 25-gauge needle; re-cap and seal the glass vial. Place the syringe vertically into the hole in the robot arm end effector tool, resting in place ready for extrusion.
4. Start the Python program, which begins slowly moving the robot arm from side to side across the range of the frame interior (the range over which fibres will be spun).
5. Gently press the syringe plunger to extrude a tiny piece of the solution from the syringe tip. Using either sharp tweezers or the experimenter’s own gloves, touch the extruded piece, allowing it to adhere and pull the piece out of the syringe. The piece will bring out a continuous fibre which can be moved onto the spinning frame below. If a good composition is chosen, the fibre will now extrude automatically from the syringe, forming fibres on the frame. Once a suitable density of fibres is attained on the frame, remove the spinner carefully and stop the robot arm program. Place the frame into a clean dry petri dish, leaving it open in the MSBC to allow any adsorbed solvent to evaporate.
6. Place the petri dish under a light microscope for characterisation of fibre quality.

The spinning technique took some trial and error, and was only automated once a consistent spinning technique had been developed by hand, with many early attempts failing to produce any fibres at all, but was eventually mastered for consistently spinnable solutions. Some compositions were always challenging to spin, breaking off quickly and not spinning for more than a few seconds, making their fibres low quality.

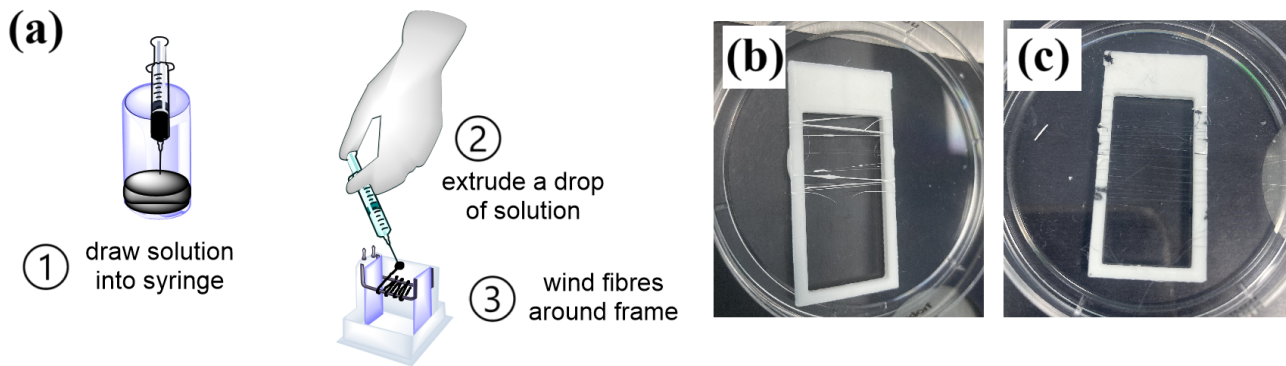


Fig. 14. (a) Steps for the manual spinning by hand. **(b)** An early attempt at spinning fibres onto a simple rectangular fixed frame, using a 30 wt% polystyrene spinning solution (no magnetic particles). The fibres were spun by hand, without the aid of a spinner or robot arm. The fibres are blobby, highly variable in thickness and some have split due to the low quality technique. **(c)** Hand-spun magnetic fibres with 20% PS and 20% iron oxide.

Calculating Fibre Width

Each frame was imaged under light microscopy at 20 \times magnification and saved as a digital image of dimensions 3226 \times 3024 pixels. A reference scale bar of size 180 μm was displayed in all images, rendered at a constant width of 711 pixels in the digital image, enabling accurate determination of the widths of the fibres. Each frame was manually moved to a number (between 2 and 6, depending on how many fibres are present) of different locations under the imaging lens to capture a representative range of the fibres within a frame. The images were then randomly sampled to produce 10 measurements along the fibres to produce an estimate of the mean and standard deviation in the fibre width. This simple data analysis was performed in Python, reading from Excel data via the `pandas` library.

Testing Magnetic Responsiveness

An electromagnet was added to the Arduino circuit board, programmed to turn the electromagnet on and off forever, at 9 V DC and limiting current draw, at 1 second intervals (50% duty cycle). A phone holder designed to fit into the robot tool holder was 3D printed. My iPhone was used for photo and video recording, using the robot arm to hold a position parallel to the frame to see deflections from the fibres. The spinner was turned off and propped up by some glass slides to give an appropriate clearance gap of approximately 2 mm above the electromagnet.

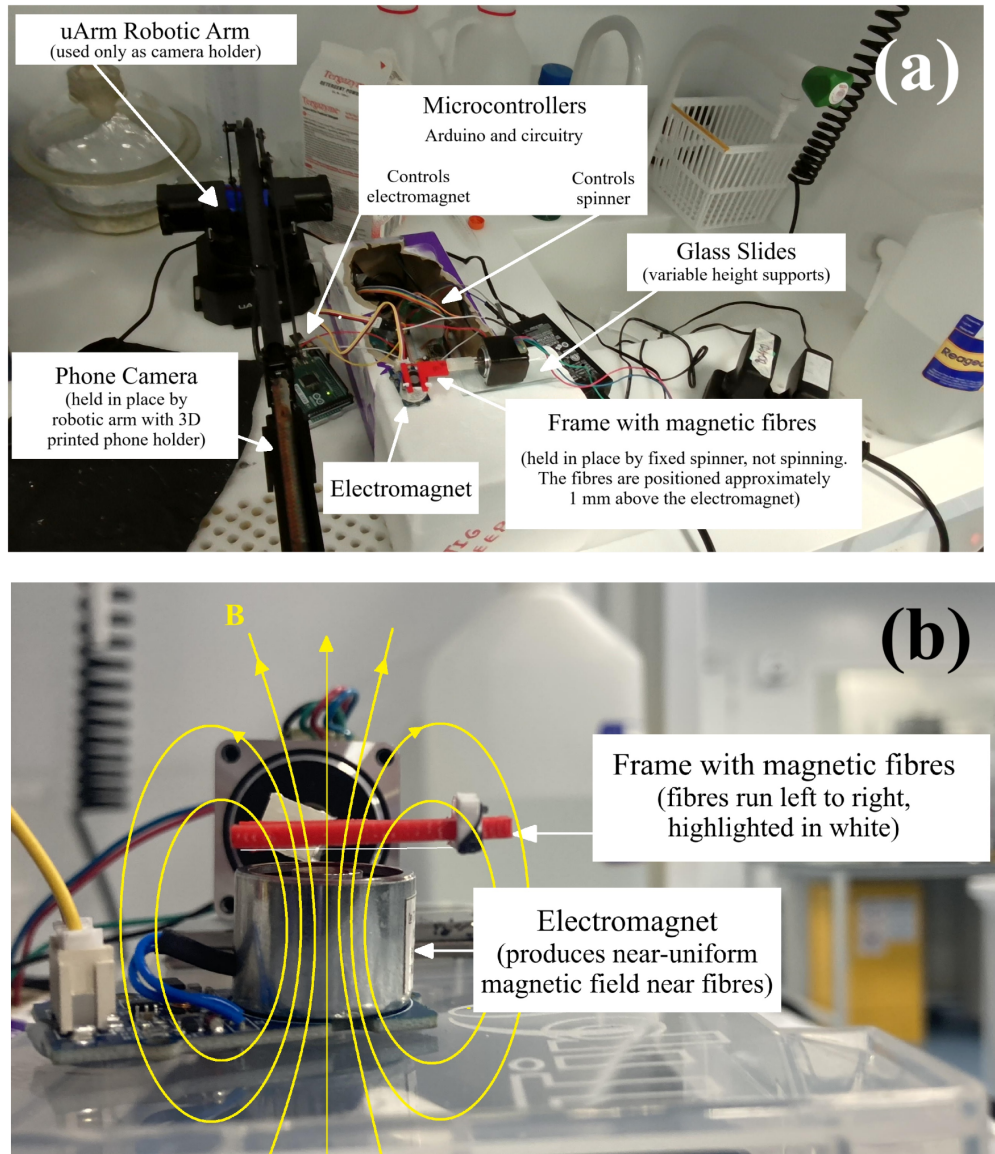


Fig. 15. (a) Overview of setup for testing deflection in a magnetic field. **(b)** Same setup, from the perspective of the phone camera, with the horizontally-oriented undeflected fibre made visible.

The frame (red in Figure 15(b)) was held horizontally at rest, with the slider (white in Figure 15(b)) at its ends, initially at full extension. A video was started and the electromagnet circuit was turned on, and five successive deflections (if visible) were observed on video before stopping. The video could then be analysed for the deflection and angle of deflection at the ends by screenshotting at key frames and reading from pixel measurements in the simple graphics editor software MS Paint. Alternatively, these calculations might be automated using computer vision and/or a programmed GUI (using e.g. Python's opencv and tkinter modules) but this was deemed unnecessarily complicated when the small number of images could more easily be processed manually, as shown in Figure 16.

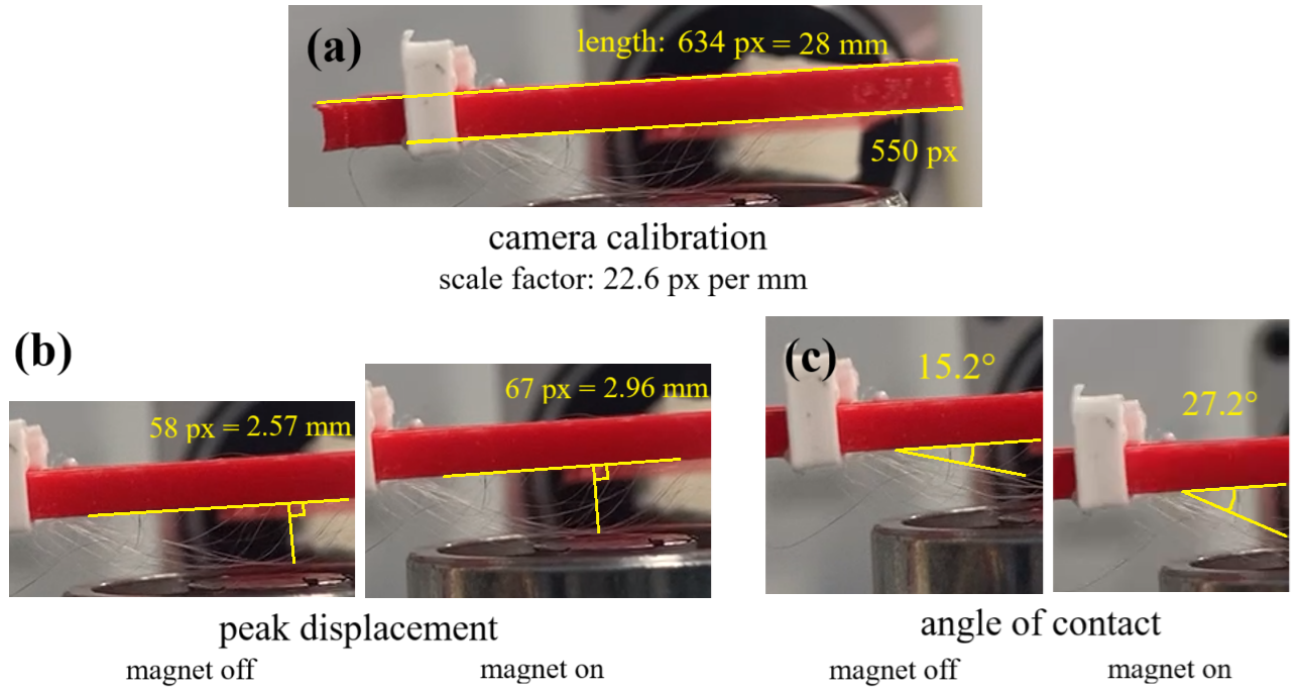


Fig. 16. (a) The scale factor for pixels to millimetres is determined by finding the distance along the full length of the frame in the image (frame is 28 mm long). The distance of the slider is also found and evaluated using this scale factor (e.g. 550 px = slider is at 24.3 mm). (b) Perpendicular lines to the frame are drawn to the point where the fibres converge in the image, at their peak displacement, and the length of this line segment is measured and converted to mm using the scale factor found above. (c) Tangent lines are drawn parallel to the fibres closest to the frame and the angle is computed using trigonometry from the pixel coordinates.

Preparing Hydrogels

The following procedure was used to prepare each fibre solution:

1. To a clean measuring cylinder, pour out 50 ml of DI water; transfer to a small beaker.
2. Place a clean dry weighing boat on a balance; tare the balance.
3. Using a spatula, weigh out the appropriate masses of gelatin and sodium alginate powder into the weighing boat. Add the contents to the beaker of DI water.
4. Drop in a large magnetic stir bar and label the beaker.
5. Place the beaker on a hot plate at 80 °C and stir at moderate power for 1 hour.
6. Remove the stir bar and transfer the beaker to a refrigerator. Once cooled to room temperature, the hydrogel will crosslink itself and transition to the single solid phase.
7. When the hydrogel is ready for use, transfer the beaker containing the solid hydrogel to an oven at 80 °C for approximately 10 minutes to melt the hydrogel into the liquid state.
8. The liquid hydrogel formulation can now be added to e.g. the 3D bioprinter or an uncapped syringe for manual deposition onto the fibres. The hydrogel will naturally solidify again as it equilibrates to room temperature.

Preparing the Fibre-Hydrogel Composites

Once the desired fibres have been spun and the hydrogels prepared, combining them together is very straightforward, and can be done manually or using a 3D printer. In this project, to save time, the composites shown in images in this report were done by hand, but the in-house 3D bioprinter Printer.HM was also able to easily print the hydrogel, ideal if using a cell culture.

1. Draw up 0.65 ml of warm liquid phase hydrogel into a 18-gauge needle-capped syringe. This can be performed shortly after removing from the oven due to the rapid natural cooling to ambient temperature.
2. Inject the hydrogel carefully on top of the fibres, one drop at a time. The high surface tension of the hydrogel can be exploited by forming small beads on the surface and joining them together to fill out the whole area above the fibres. Ensure that a small region near the slider is left clear.
3. Wait for approximately 10 minutes for the hydrogel to solidify on the fibres. The hydrogel can be gently pressed with a non-stick surface to ensure good adherence.

Testing the Fibre-Hydrogel Composites for Magnetic Responsiveness

Due to the damage induced by testing the flexibility of the pure fibres (shown in Figure 13(a)), a new set of fibres was spun from the same solutions when testing the fibres with the hydrogel. The solution (contained within a small vial) was reheated at 50 °C on a hot plate and the magnetic stirring was turned on. No stir bars were inside the vials, but the magnetic solutions were able to spin to some extent on their own. This was performed to solubilise any precipitated polymer ‘blobs’ which were observed to develop from dried-out solutions, although visibility was obscured by the opaque black iron oxide coating on the vial interior. To save time, these were spun by hand by manually extruding from a 25-gauge blunt-tipped syringe. Due to developing more practice throughout the course of the project, the hand-spinning technique shown in Figure 17 had improved in quality significantly from that shown in Figure 14(c).

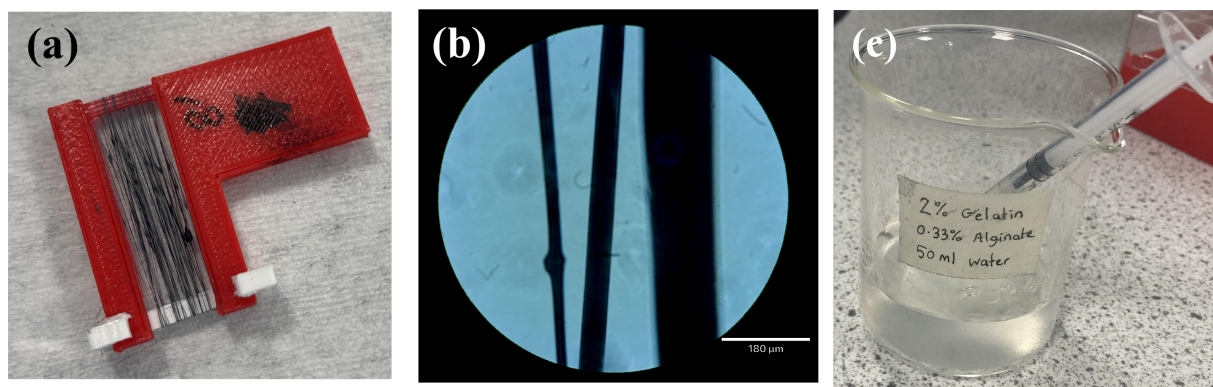


Fig. 17. (a) New fibres spun by hand (no spinner, no robot arm, no added hydrogel) using Composition (8), after reheating the solution at 50 °C for 10 minutes with gentle stirring.

- (b)** Microscopy of hand-spun fibres from Composition 8, showing larger-than-normal variation in fibre thickness (scale bar: 180 µm) and a small blob on one of the fibres is visible.
- (c)** Hydrogel (2) in its solid state, to be heated before deposition onto the fibres.

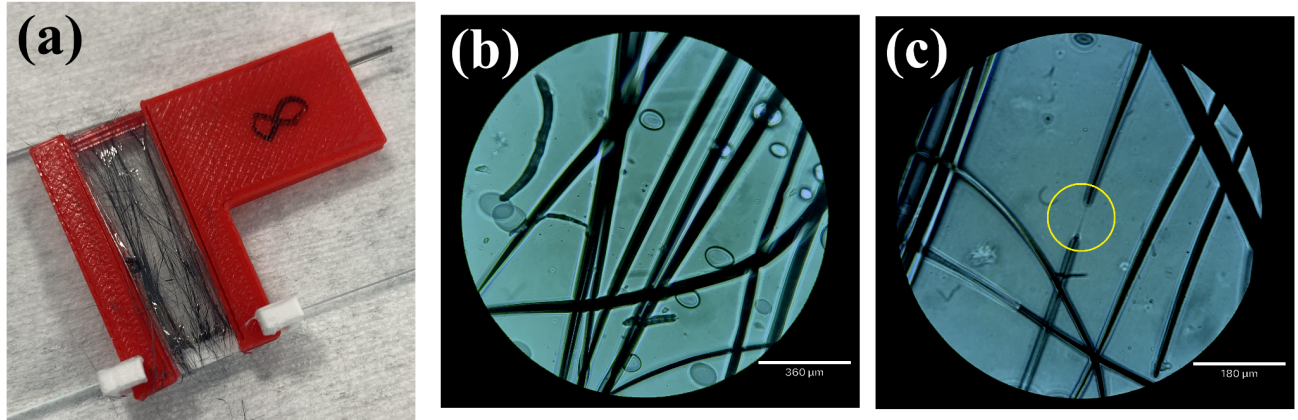


Fig. 18. **(a)** The old fibres from Composition (8) were severely frayed after repeatedly changing the length (by moving the white slider) and actuating with the magnet, then ‘freezing’ with hydrogel (1), giving a very rigid composite with no practical use. **(b)** Microscopy at 10× resolution (scale bar: 360 µm) of these fibres, showing many defects and tangled fibres. **(c)** Another close-up at 20× resolution (scale bar: 180 µm). In the yellow circled region, the fibre has become partially uncoated, losing a section of the iron oxide sheath and leaving a tiny barely-visible strand of polystyrene (diameter ~ 1 µm).

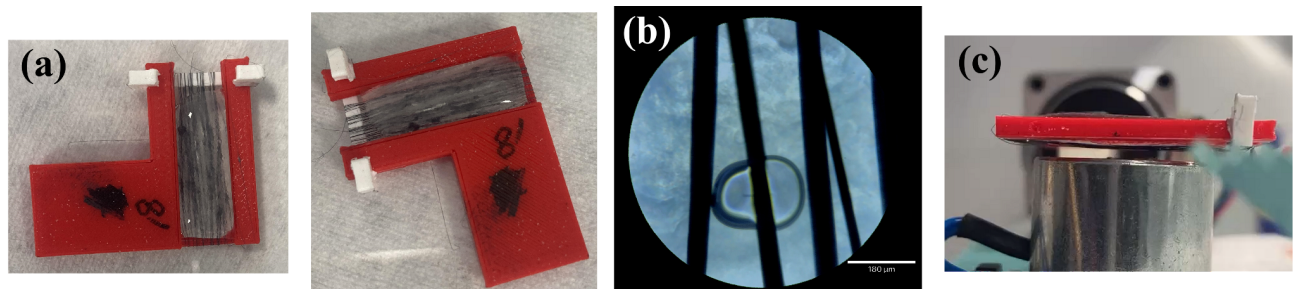


Fig. 19. **(a)** The hydrogel-fibre composite, using the new Composition (8) and hydrogel (2). The slider is in the fully extended position. **(b)** Microscopy of the fibre-hydrogel composite, observed from above. The scale bar reads 180 µm. A tiny spherical air bubble in the hydrogel is visible. **(c)** The fibre-hydrogel composite on the frame ready for testing with the electromagnet. The fibres are along the bottom and the hydrogel extends up to the top.

(5) Results and Discussion

Trialed Compositions

The first tested composition used 30 wt% PEO, initially without addition of magnetic particles, in the 85:15 DMF:acetone solvent. Unfortunately this composition produced a highly gummed-up solution with phase separation in mixture even after heating, and no fibres could be pulled from the system. A second trial using 20% PEO and 20% iron oxide in the same solvent yielded a similarly useless product. The second tested composition used 20% PU mixed with 20% PEO, in which it was expected that PEO might be able to help enhance the spinnability of PU [21], but this was also unsuccessful, and the solvent was unable to dissolve the PU.

Polystyrene gave generally much better results, with many proportions yielding readily spinnable fibres. It was noted that compositions with 20-30% PS performed the best, and could be combined iron oxide up to a solid proportion of approximately 50%. Nine different compositions of PS-based fibre solutions were prepared, as shown in Table 5.

Identifier	Polystyrene, wt%	Iron oxide, wt%	Solvent
(1)	10	10	
(2)	20	10	
(3)	30	10	
(4)	10	20	
(5)	20	20	85 v% DMF + 15 v% acetone
(6)	30	20	
(7)	10	30	
(8)	20	30	
(9)	30	30	

Table 5. Compositions of the nine fibre solutions prepared and studied.

The gelatin-alginate hydrogels required careful control of the resulting hydrogel stiffness in order to facilitate actuation in the composite. Table 6 shows the three hydrogel compositions trialled in this project. It was found that when hydrogel (A) was added to the frame, the whole frame became too rigid for the fibres to move: they were effectively frozen in place. More compliant hydrogels were necessary for observable actuation, and (B) was found as the minimal

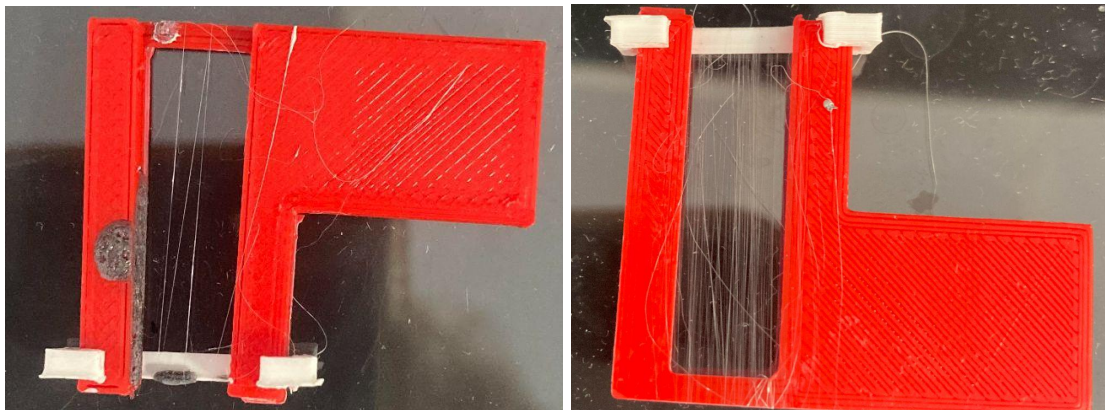
concentration such that the UCST (i.e. solidification temperature) of the gelatin-alginate hydrogel was just above room temperature, ensuring a mechanically flexible hydrogel. Composition (C) was too dilute to form a hydrogel, with its UCST close to the freezing point of water, remaining in its gel (two-phase liquid) state down to room temperature, and so could not be used with any fibres.

Identifier	Gelatin, wt%	Sodium alginate, wt%	Solvent
(A)	6	1	DI water
(B)	2	0.333	DI water
(C)	0.25	0.083	DI water

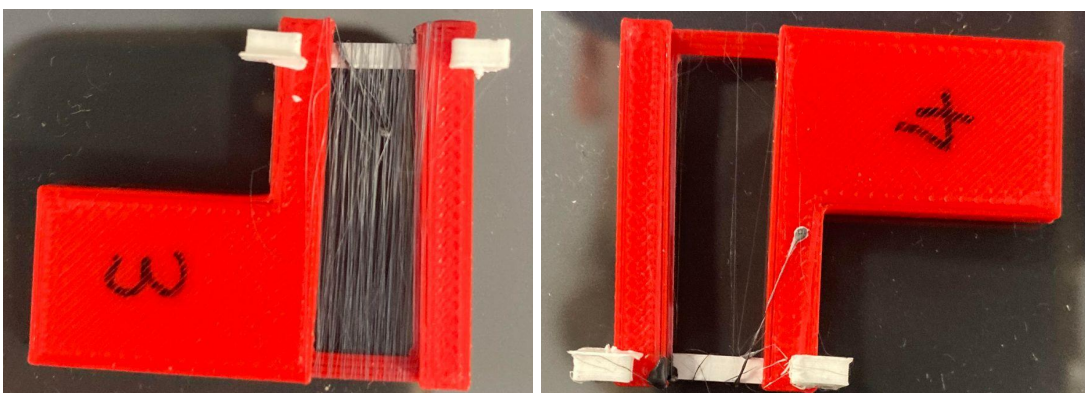
Table 6. Compositions of three hydrogels tested, (A), (B) and (C).

Spun Fibres

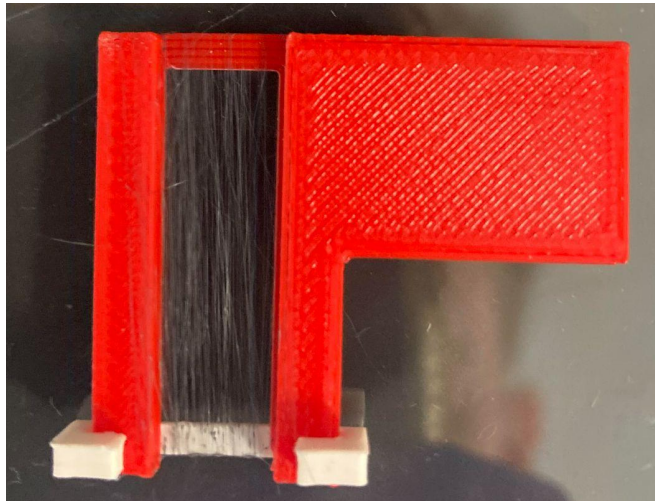
The fibres from each composition (1)-(9) (defined in Table 5) were spun at full length.



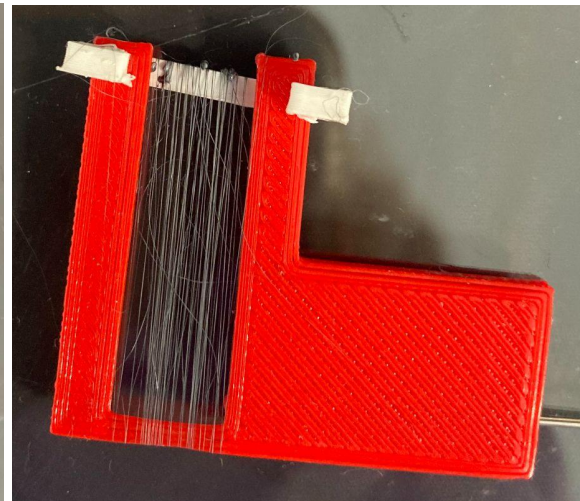
Composition (1)
10% Polystyrene, 10% Iron Oxide **Composition (2)**
20% Polystyrene, 10% Iron Oxide



Composition (3)
30% Polystyrene, 10% Iron Oxide **Composition (4)**
10% Polystyrene, 20% Iron Oxide



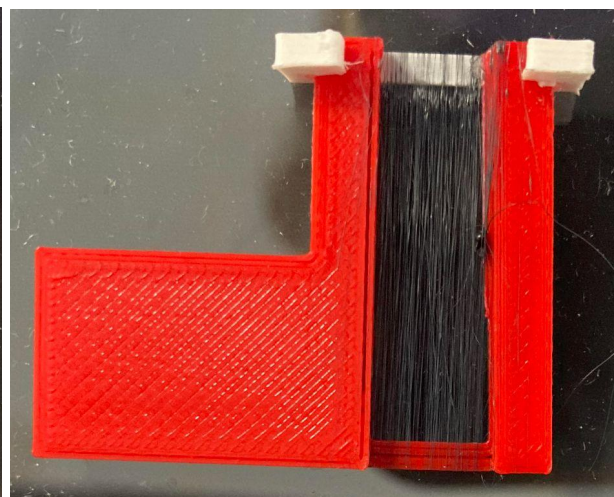
Composition (5)
20% Polystyrene, 20% Iron Oxide



Composition (6)
30% Polystyrene, 20% Iron Oxide



Composition (7)
10% Polystyrene, 30% Iron Oxide

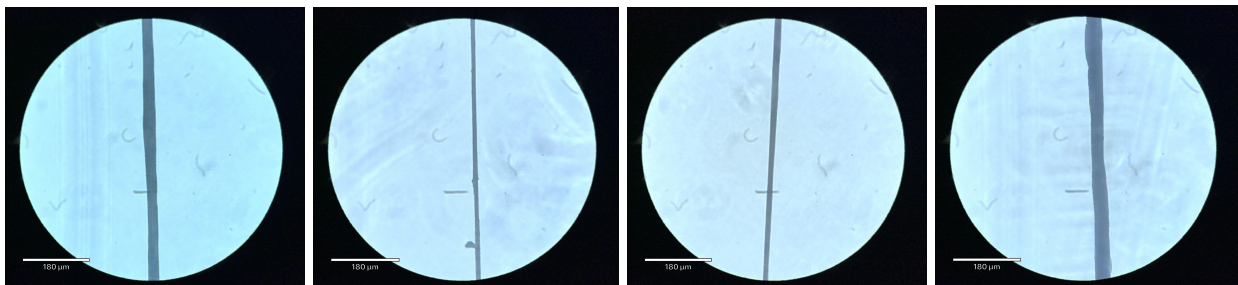


Composition (8)
20% Polystyrene, 30% Iron Oxide

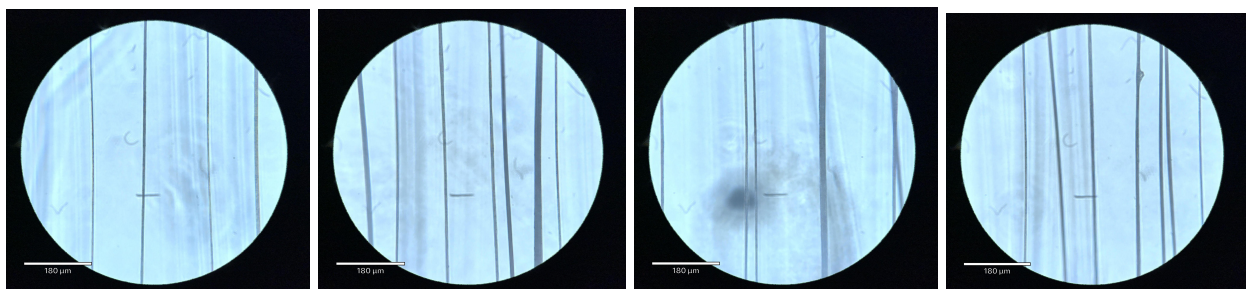
Visually, compositions (3), (5), (6), (7) and (8) produced good-quality fibres. (1) and (4) were extremely fragile and broke off rapidly during extrusion. (2) was also fragile but a little better. The solvent solution used to produce Composition (9) (30% Polystyrene, 30% Iron Oxide) was a practically-solid solution from which drawing up any remaining solvent into the syringe was impossible, even when reheated to 80 °C. Therefore, no fibres could be spun from (9) and it was removed from the subsequent investigations.

Microscopy and Characterisation

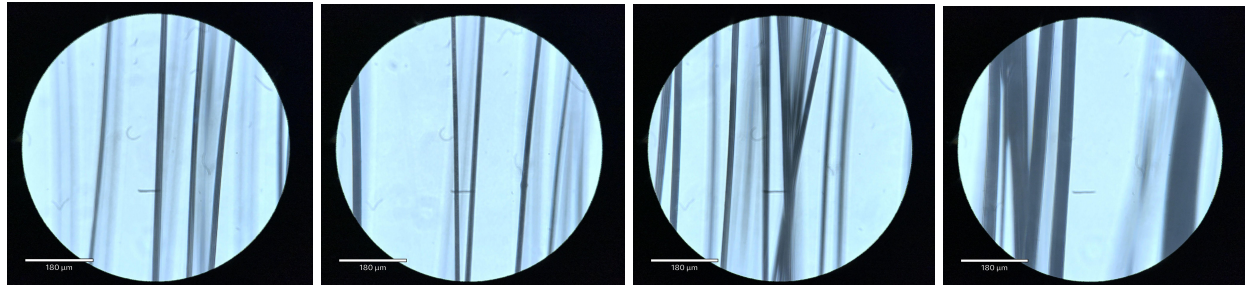
Light microscopy at 20 \times magnification. The scale bar in all images reads ‘180 μm ’.



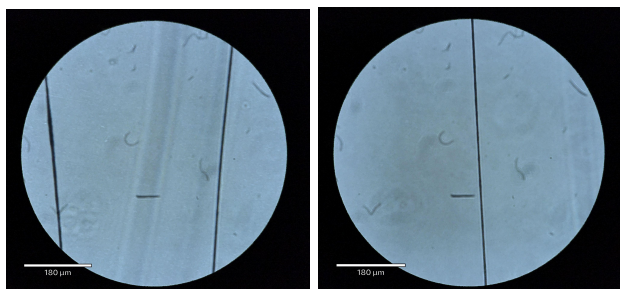
Composition (1): 10% Polystyrene, 10% Iron Oxide



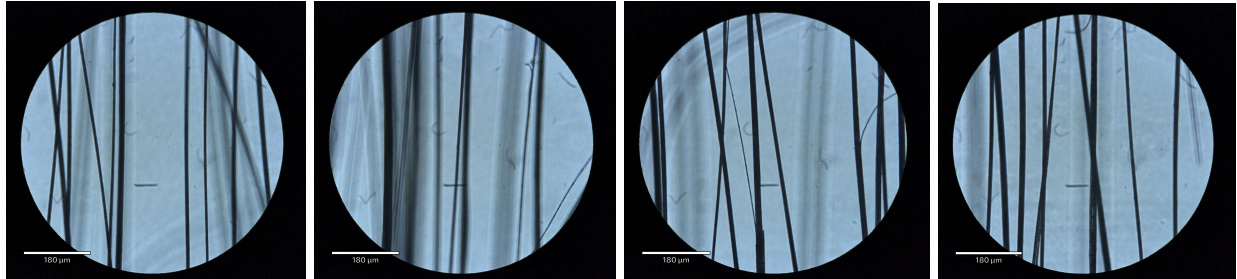
Composition (2): 20% Polystyrene, 10% Iron Oxide



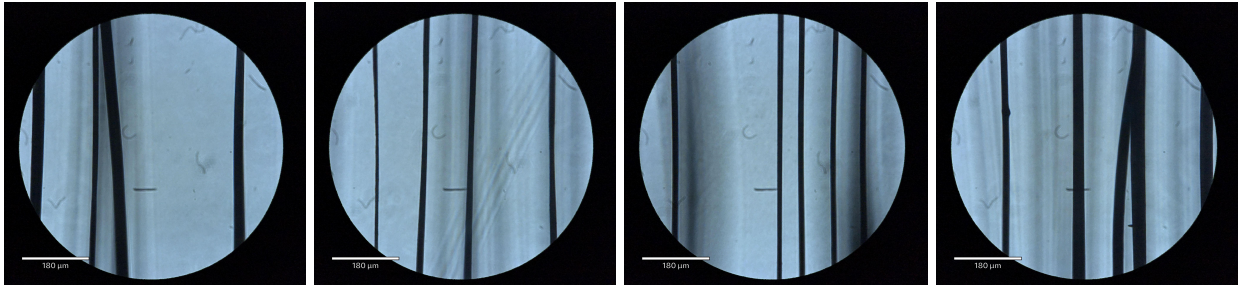
Composition (3): 30% Polystyrene, 10% Iron Oxide



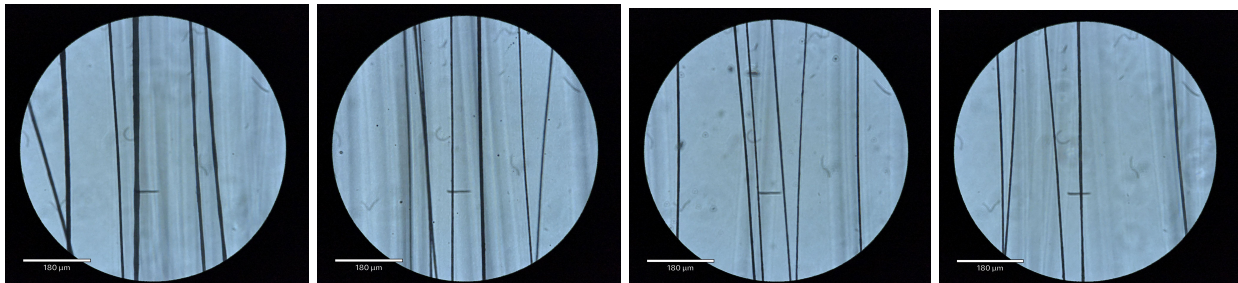
Composition (4): 10% Polystyrene, 20% Iron Oxide



Composition (5): 20% Polystyrene, 20% Iron Oxide



Composition (6): 30% Polystyrene, 20% Iron Oxide



Composition (7): 10% Polystyrene, 30% Iron Oxide



Composition (8): 20% Polystyrene, 30% Iron Oxide

As mentioned previously, Composition (9) yielded no fibres so there was nothing to examine.

Fibre Widths

Some additional microscopy photos other than those shown above were taken to gather more data, and each image was randomly sampled, forming a dataset of the widths of the fibres from each sample, collecting 10 data points for each composition.. The bar charts in Figure 20 show the mean and standard deviations (as error bars).

Number of samples	Mean	Standard deviation	Minimum	Maximum
80	14.8 μm	8.7 μm	4.1 μm	40.0 μm

Table 7. Summary statistics for the whole dataset of fibre diameters.

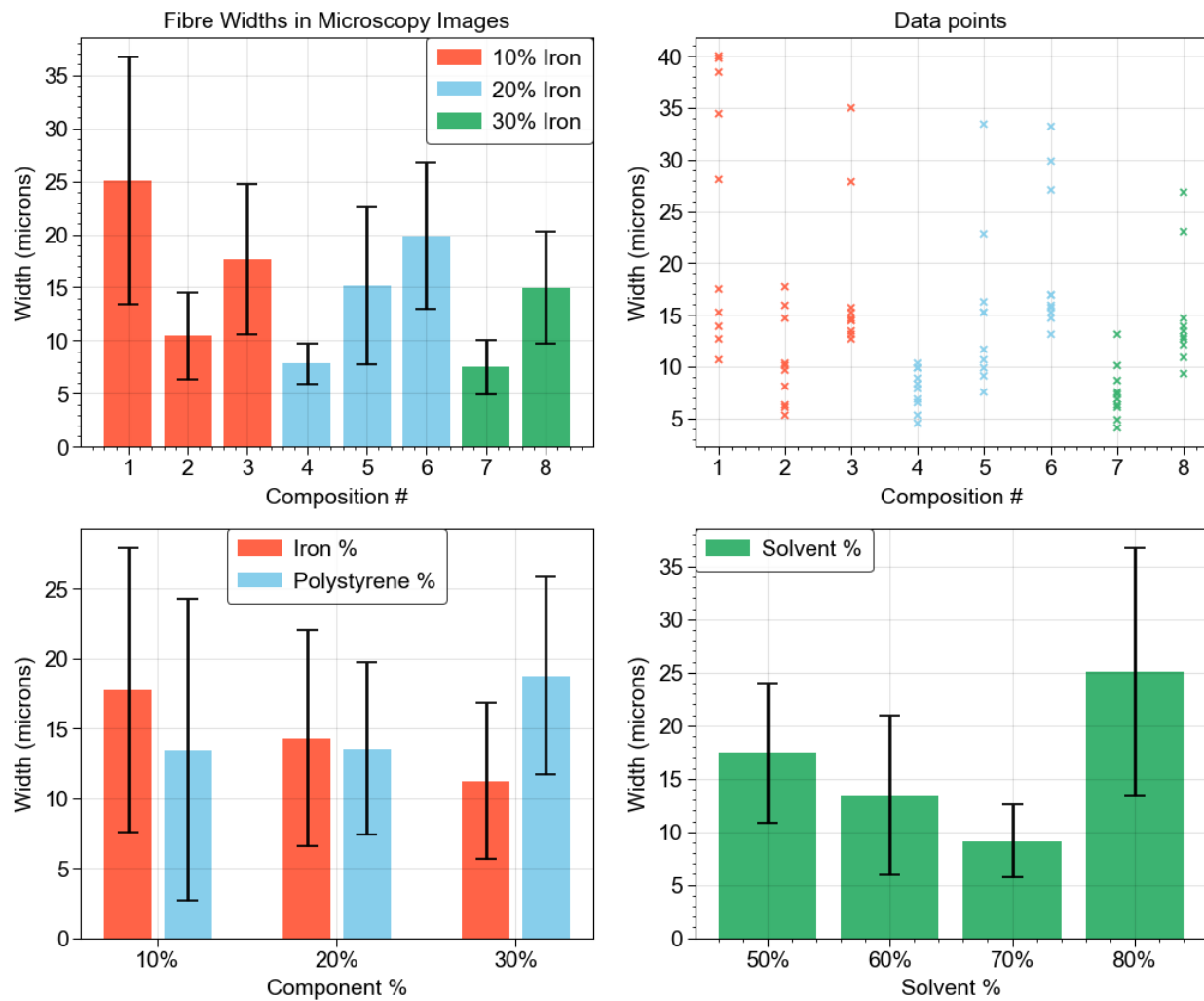
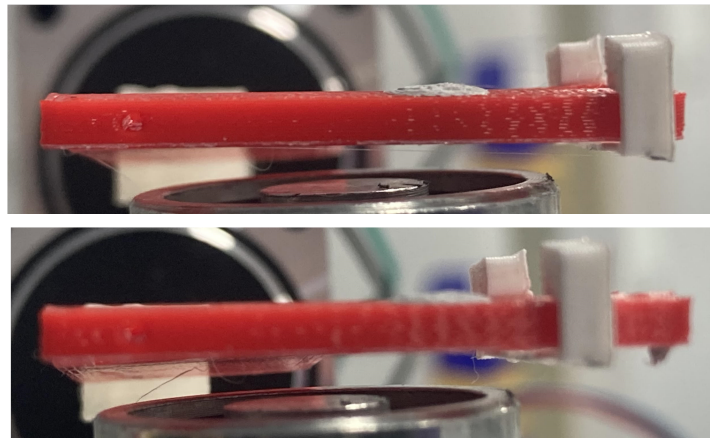


Fig. 20. Data showing the variation of fibre diameter for all compositions, before the addition of any hydrogel and before testing for magnetic response. The error bars show plus or minus one standard deviation for each group.

Fibre Magnetic Actuation (No Hydrogel)

Each frame was held above the electromagnet. In the photo below of testing Composition (1), the **top** image shows the frame at fully extended length, at which deflection is minimal (invisible). The **bottom** image then shows the frame with the slider slightly contracted by approximately 1-3 mm, and the measurements are analysed.

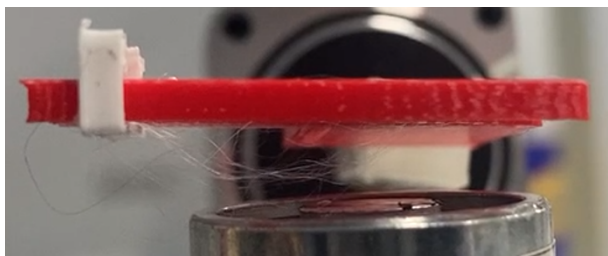


Compositions (1) and (4) (effectively the same response, too fragile to investigate)

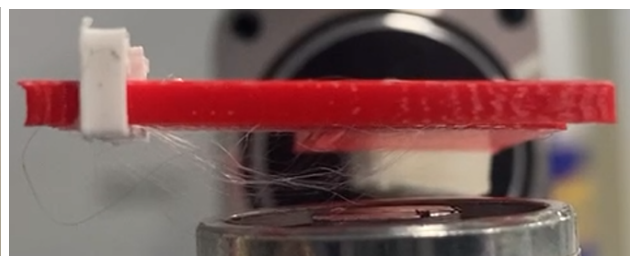
In each of the following, the slider was contracted a very small distance and photos were taken during the period when the electromagnet was on and off. The motion can be better observed on video, but analysis of the photos is also used to quantitatively determine deflections and angles.



Fully extended, electromagnet **on/off** (no visible deflection)

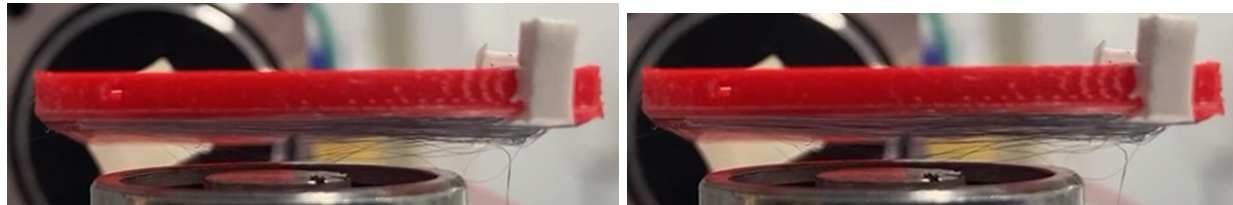
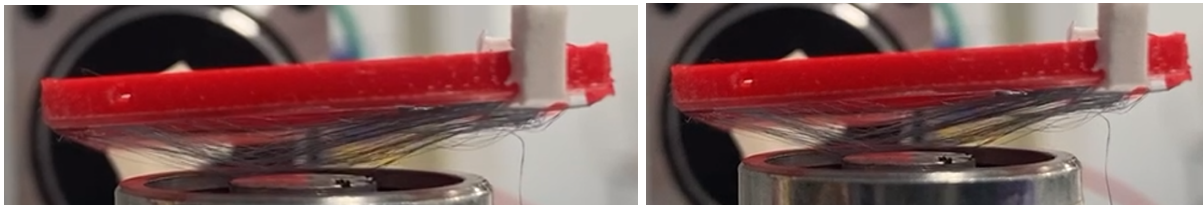
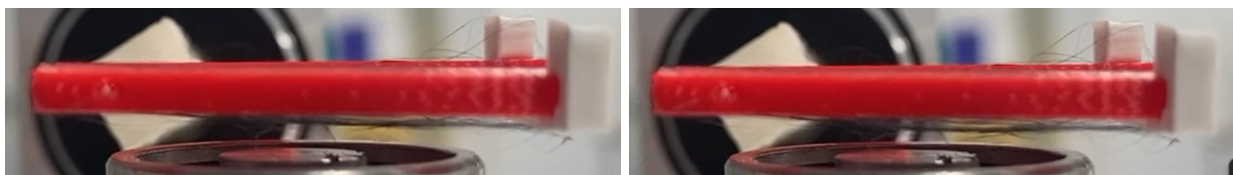
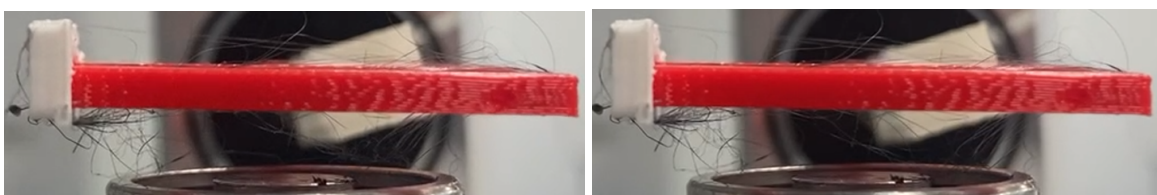
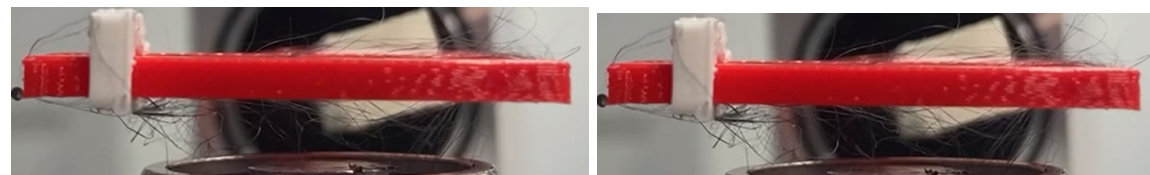


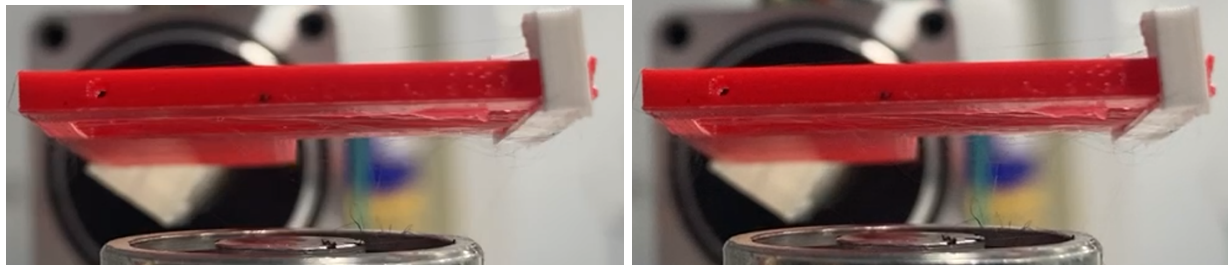
Contracted, electromagnet **off**



Contracted, electromagnet **on**

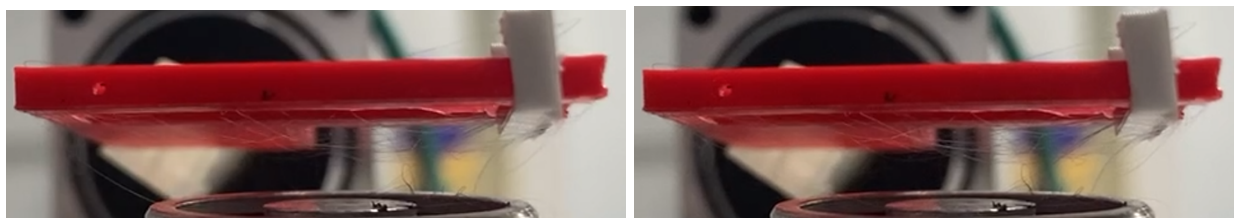
Composition (2) (also poor quality, but deflection is observed without breakage)

Fully extended, electromagnet **off**Fully extended, electromagnet **on**Contracted, electromagnet **off**Contracted, electromagnet **on****Composition (3)**Fully extended, electromagnet **off**Fully extended, electromagnet **on**Contracted, electromagnet **off**Contracted, electromagnet **on****Composition (5)**Fully extended, electromagnet **off**Fully extended, electromagnet **on**Contracted, electromagnet **off**Contracted, electromagnet **on****Composition (6) (unfortunately fibres became damaged due to experimental error)**



Fully extended, electromagnet off

Fully extended, electromagnet on



Contracted, electromagnet off

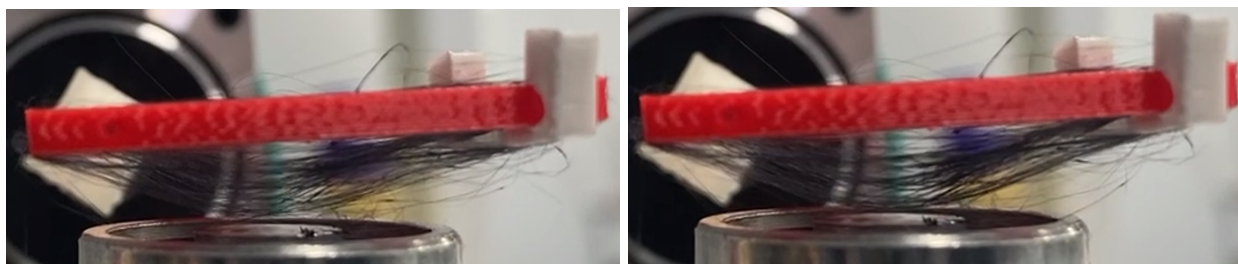
Contracted, electromagnet on

Composition (7) (thin fibres are hard to see, but actuation is clear on video)



Fully extended, electromagnet off

Fully extended, electromagnet on



Contracted, electromagnet off

Contracted, electromagnet on

Composition (8) (very clear actuation, best performing fibres)

Maximum Displacements and Angles of Contact of Fibres (No Hydrogel)

Videos were captured of each set of fibres, switching the electromagnet on and off every second. The peak deflection of the fibres and the angle of contact with the supports of the frame were recorded by counting pixel distances on the images at each ‘on’ and ‘off’ interval, providing a data point for each variable per one second of video. Since sample (1) and (6) were destroyed by the magnet, it could not be recorded. (4) remained intact and could be measured albeit with only one single fibre and its angle could not be measured. The results are shown in Figure 21.

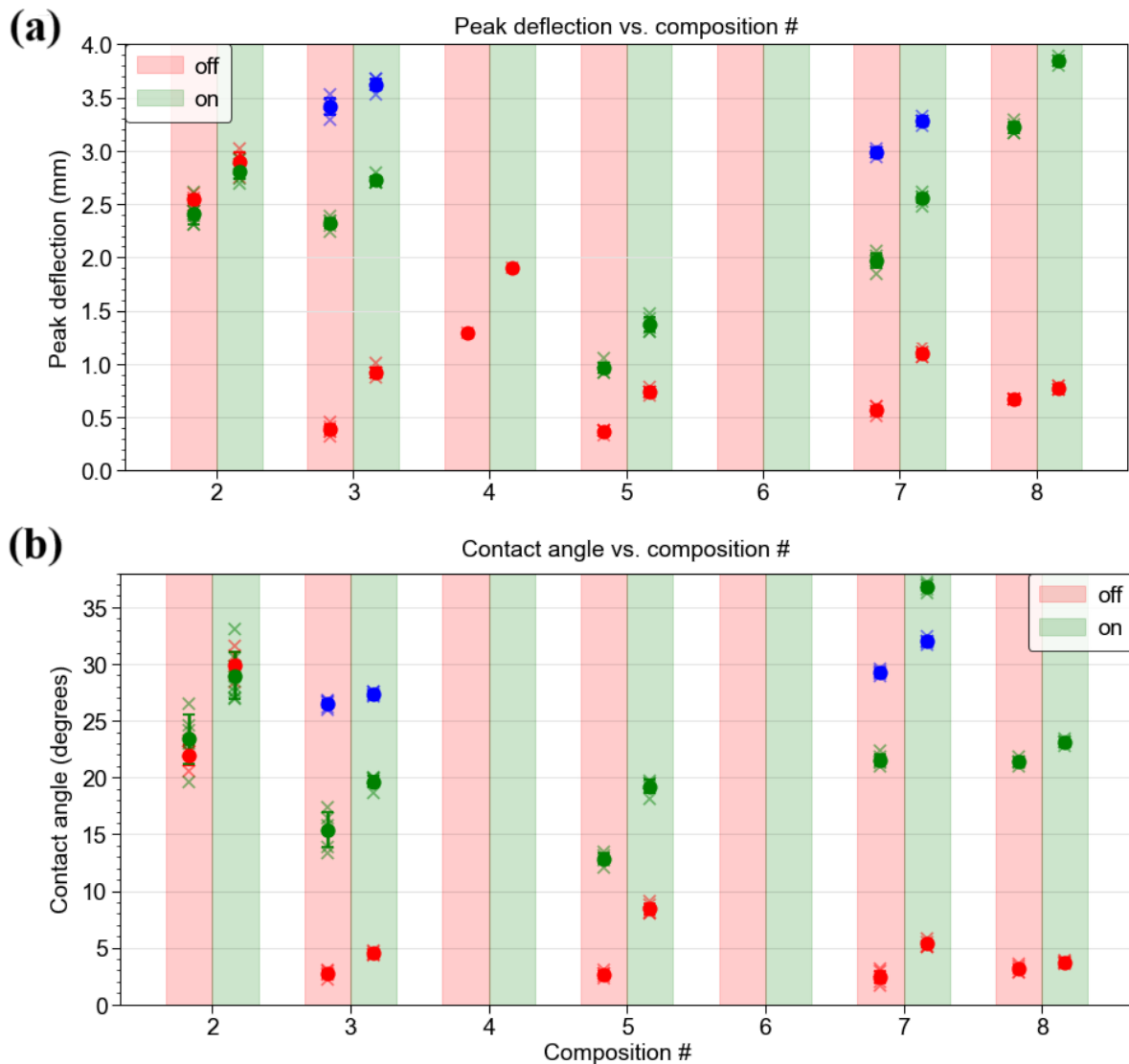


Fig. 21. (a) Peak deflections and **(b)** contact angle with supports of the fibres of each composition, with red and green columns for electromagnet ‘off’ and ‘on’ respectively, shown as $N = 5$ data points (\times) as well as mean (\bullet) and standard deviation as error bars. The key to the marker colour (represents different slider distances) is given in Table 7.

Colour	Composition #						
	2	3	4	5	6	7	8
red	24.39	26.63	28.00	28.00		27.66	27.85
green	25.38	25.84		26.28		25.86	27.15
blue		23.44				25.94	

Table 7. The values of the fibre horizontal length (distance to slider) in mm, corresponding to the datasets of each marker colour in Figure 15. For example, the red markers in Composition (2) were collected at a slider distance of 24.39 mm.

Fibre Magnetic Actuation (With Hydrogel)

The new fibres from Composition (8) with hydrogel (2) were actuated. As before, the photo format makes direct comparison visually difficult but the actuation is very clear on video.



Fully extended, electromagnet **off**



Slightly contracted, electromagnet **off**



Slightly contracted, electromagnet **on**

It is noted that the fibres are pulled down towards the electromagnet to a lesser extent than without the hydrogel, as predicted by the theoretical composite model discussed in Section 3.1. Additionally, it can be seen in Figure 22, by observing the top section of the frame, the hydrogel is also pulled down by a similar distance as the fibres, indicating that the composite indeed moves as a collective unit, without delamination of the fibres from the hydrogel matrix. This also verifies the feasibility of actuating the hydrogel remotely since the fibres are not in physical contact with the electromagnet at any point during the motion.

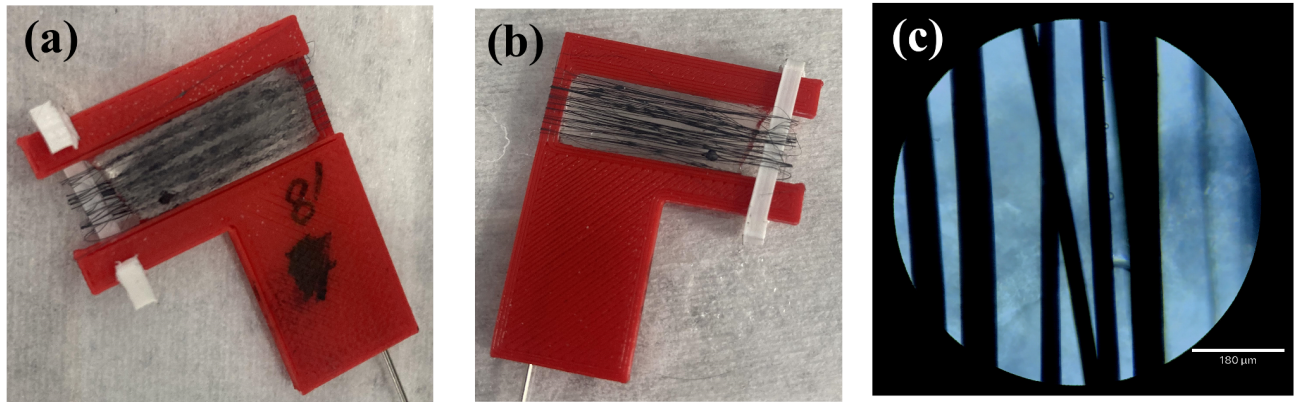


Fig. 22. (a) The frame containing the fibre-hydrogel composite after performing the actuation tests. The quality of the fibres is retained, unlike in the case without the hydrogel, where the testing step significantly degraded the fibres. The hydrogel has not shifted position and the slider is still in the slightly contracted position, so the fibres around the edge are a little loose, but are easily straightened up by pulling the slider back gently to the fully extended position.
(b) The bottom side of the frame, showing that the fibres are still fully intact on both sides.
(c) Microscopy confirms that the fibres are still of good quality, without breakage. Some tiny air bubbles in the hydrogel are still present, similar to before testing (as seen in Figure 14).

Angles and Deflection and Maximum Displacements of Fibres (With Hydrogel)

A total of 40 seconds of video was captured of the fibres from Composition (8) with hydrogel (2), providing 20 measurements each where the electromagnet was ‘on’ and ‘off’ respectively, allowing for analysis of the change in peak displacement and change in contact angle with the supports for both the fibres (bottom of the frame) and the hydrogel (top of the frame). The results are shown in Figure 23. The fibres were spun at a length of 26.5 mm and the slider was contracted by 1.0 mm to a distance of 25.5 mm where all measurements in Figure 23 were taken.

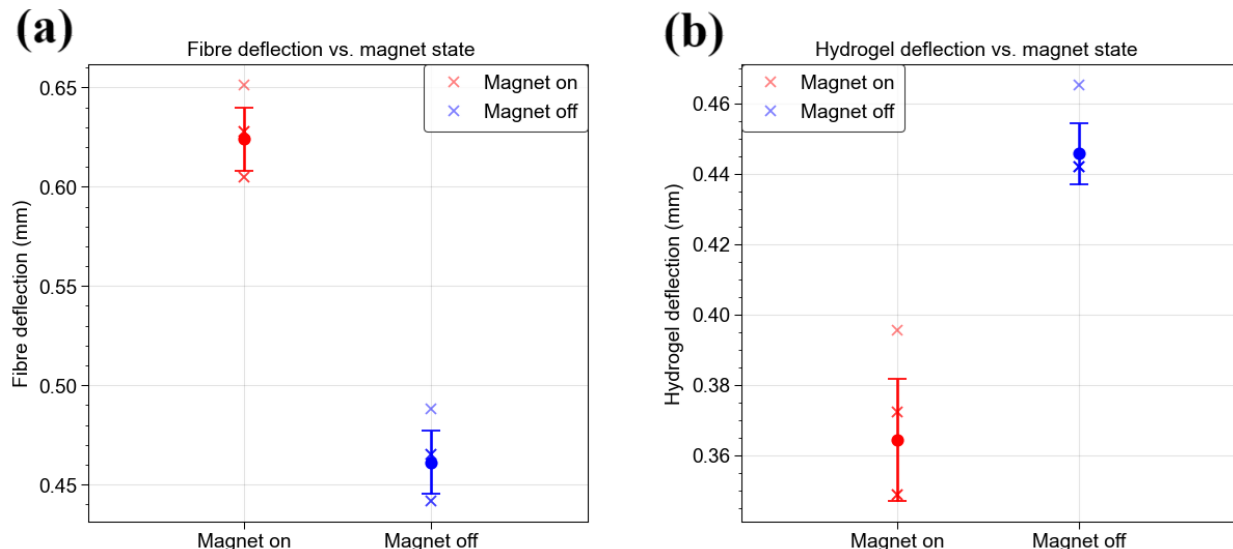


Fig. 23. (a) Peak deflection of the fibres observed at the bottom of the frame. (b) Peak deflection of the hydrogel observed at the top of the frame. In both, $N = 6$ data points were collected for each case (magnet on and off).

The change in peak displacement caused by the magnet is shown in Table 8, showing the mean change μ and standard deviation in change. It is observed that the mean displacement of the hydrogel is approximately half that of the fibres, suggesting that the hydrogel partially deforms as well as the fibres. A statistical analysis of the data was performed to explore the difference between the ‘magnet on’ and ‘magnet off’ states. This verifies that the deflection is due to the magnet rather than noisy data at the 5% significance level, using a two-tailed Student’s t -test for independent means in the two categories. The p -value for the fibre and the hydrogel is also shown in Table 8.

Fibres			Hydrogel		
μ [mm]	σ [mm]	p -value	μ [mm]	σ [mm]	p -value
0.163	0.027	1.76×10^{-8}	0.081	0.012	2.82×10^{-6}

Table 8. Displacements caused by magnet acting on composite.

Although small compared to the frame, these deflections are visible to the naked eye and are well-captured on video. If the hydrogel were to be loaded with a seeding of cells, as is common in its target application, these cells would experience displacements approximately 5-10 times their diameter, providing a relatively large mechanical stimulus to the cells. With more powerful magnets, larger deflections could be easily achieved, although further analysis and experimentation would be needed to ensure this does not lead to failure of the fibres or hydrogel, as the larger stresses would render the fibres prone to fatigue failure and cutting of the hydrogel.

(6) **Conclusions**

6.1. Primary Findings

This project has developed a novel composite material comprising magnetic fibres in a soft hydrogel matrix using the nanospinning technique, and has presented several key findings that could contribute to the advancement of soft actuator technology, as outlined below.

1. Automated Nanospinning:

- The project successfully demonstrated the use of an open-source robotic arm and motor-controlled spinner to achieve automatic extrusion of nanofibres.
- This manufacturing process ensures precise control over the spinning parameters, resulting in consistent microfibers with an average diameter of 15 ± 9 microns, which is much smaller than many current magnetic fibres known in the literature.
- The ability to automate the process enables high-throughput production of magnetic microfibers, making it suitable for scalable manufacturing.

2. Solvent Selection:

- A binary solvent comprising 85% DMF and 15% acetone was identified as the optimal solvent for the magnet-polymer mixture.
- This solvent system effectively dissolves the mixture, allowing for efficient spinning and improved fiber properties.

3. Iron Oxide and Polystyrene Concentrations:

- Experiments were conducted varying the iron oxide and polystyrene concentrations on the spinnability and magnetic responsiveness of the microfibers.
- Results find a 40-50 wt% solid fraction yielded spinnable solutions, with the highest magnetic responsiveness observed at the highest iron content.
- A solution comprising 20% PS and 30% iron oxide yielded the best performing fibres with respect to both spinnability and magnetic responsiveness.

4. Deflection Tests and Hydrogel Integration:

- Deflection tests demonstrated peak transverse strains of up to 7% (2 mm) with no time delay in deflection or observable loss over time, indicating the rapid and efficient actuation of the microfibers.
- The integration of a minimally-stiff hydrogel into the system was straightforward once the ideal composition was identified, and did not significantly affect the actuation performance, demonstrating mechanical compatibility with hydrogel phase.
- These results underscore the potential of the microfibers for use as soft actuators in applications requiring precise and controlled movements.

5. Optimal Performance:

- The composite using 20% PS and 30% iron oxide was actuated over approximately 50 cycles with no observable decline in performance, although quantitative analysis of this claim was not performed and relied only on observations. Longer-term studies with thousands of cycles would also be necessary to support this conclusion.
- This composition exhibited strong adhesion to the hydrogel, overcoming common challenges faced by fibrous composites such as delamination from the hydrogel or cutting through the substrate.

6.2. Future Work

The research conducted in this project has realisable practical applications in the development of soft actuators with enhanced durability and integration capabilities in biomedical and nanoscience applications. In addition to the initial goals of forming fully 3D compatible cell-loaded hydrogel composites as discussed in Section 2.2, two main potential applications of the materials developed in this project are presented below.

Organoid Research

Organoids constitute bioengineered structures that closely imitate the architectural features and functional attributes of various human organs, typically incorporating stem cells to exploit their natural self-organisation and differentiation within an engineered model tissue, to yield an ‘organ-on-a-chip’ system. When patient-specific stem cells are used, the revolutionary field of personalised medicine can be equipped with ‘patient-on-a-chip’ models, enabling integration with powerful analytical techniques including deep learning algorithms. These complex biomimetic systems are themselves used in diverse fields such as microfluidics, drug delivery, and tissue engineering relevant to both academia and biotechnology/biomedical industry. Recently, a bioinspired *in vitro* lung model was developed with the goal of studying the transport phenomena of cells and extracellular microparticle precipitates under cyclic stress loadings, in order to emulate the tissue expansion and contraction present in lung tissue during normal breathing [30]. This study utilised physical contact forces on a poroelastic membrane to actuate the system, which places limitations on its realism *in vivo* as well as limiting biocompatibility. Incorporating the techniques developed in this project could equip the model with remote, non-contact magnetic actuation without affecting the biocompatibility of the soft material, and could facilitate scale-up by replacing the fabrication process with automated 3D bioprinting.

Biomedical Materials and Textiles

In medicine, post-surgical cavities resulting from the resection of soft tissues damaged by trauma can lead to complications due to adhesions in the internal tissues. A potential strategy to reduce the complications associated, is through filling large resection cavities with a hydrogel construct

exhibiting tissue-mimic physical properties. An ideal hydrogel construct should be injectable to comply with surgical procedures, forming a complex shape fitting into the cavity post injection, with good tissue interface. The magnetic hydrogel composite developed in this project are remotely deformable in which a practitioner could use a magnet to guide the shape of a soft material into cavities and support the tissues, reducing the risks of requiring multiple rounds of surgery. The potential to incorporate the techniques of tissue engineering remains, potentially filling the cavities using personalised tissues.

These applications demonstrate the versatility and potential of magnetic hydrogel composites in various fields. The benefits of remote non-contact actuation, enhanced tissue interface, and the potential for integration with personalised medicine leverage the unique properties of the system, allowing researchers and healthcare professionals alike to explore new avenues for advancements in bioengineering and medical technology.

(7)

References**Citations**

- [1] Utech, S., & Boccaccini, A. R. (2015). A review of hydrogel-based composites for biomedical applications: enhancement of hydrogel properties by addition of rigid inorganic fillers. *Journal of Materials Science*, 51(1), 271–310. <https://doi.org/10.1007/s10853-015-9382-5>
- [2] Liu, J., Garcia, J., Leahy, L. M., Song, R., Mullarkey, D., Fei, B., Dervan, A., Shvets, I. V., Stamenov, P., Wang, W., O'Brien, F. J., Coleman, J. N., & Nicolosi, V. (2023). 3D printing of multifunctional conductive polymer composite hydrogels. *Advanced Functional Materials*, 33(37). <https://doi.org/10.1002/adfm.202214196>
- [3] Brunsen, A., Utech, S., Maskos, M., Knoll, W., & Jonas, U. (2012). Magnetic composite thin films of Fe_xO_y nanoparticles and photocrosslinked Dextrans Hydrogels. *Journal of Magnetism and Magnetic Materials*, 324(8), 1488–1497. <https://doi.org/10.1016/j.jmmm.2011.11.039>
- [4] Salahuddin, B., Aziz, S., Gao, S., Hossain, Md. S., Billah, M., Zhu, Z., & Amiralian, N. (2022). Magnetic hydrogel composite for wastewater treatment. *Polymers*, 14(23), 5074. <https://doi.org/10.3390/polym14235074>
- [5] Tang, S., Yan, Y., Lu, X., Wang, P., Xu, X., Hu, K., Yan, S., Guo, Z., Han, X., Zhang, F., & Gu, N. (2024). Nanocomposite magnetic hydrogel with dual anisotropic properties induces osteogenesis through the NOTCH-dependent pathways. *NPG Asia Materials*, 16(1). <https://doi.org/10.1038/s41427-024-00535-x>
- [6] Yang, L., Nandakumar, D. K., Miao, L., Suresh, L., Zhang, D., Xiong, T., Vaghasiya, J. V., Kwon, K. C., & Ching Tan, S. (2020). Energy harvesting from atmospheric humidity by a hydrogel-integrated ferroelectric-semiconductor system. *Joule*, 4(1), 176–188. <https://doi.org/10.1016/j.joule.2019.10.008>
- [7] Wang, Y., Zhang, W., Shan, Y., Yu, X., & Chen, K. (2023). Preparation of polyacrylamide/calcium alginate@ $\text{Ti}_3\text{C}_2\text{T}_x$ composite hydrogels with high adhesive performance for flexible supercapacitor electrolytes. *Colloids and Surfaces A: Physicochemical and Engineering Aspects*, 666, 131312. <https://doi.org/10.1016/j.colsurfa.2023.131312>
- [8] Thoniyot, P., Tan, M. J., Karim, A. A., Young, D. J., & Loh, X. J. (2015). Nanoparticle–Hydrogel Composites: Concept, design, and applications of these promising, Multi-Functional Materials. *Advanced Science*, 2(1–2). <https://doi.org/10.1002/advs.201400010>
- [9] Simińska-Stanny, J., Nizioł, M., Szymczyk-Ziółkowska, P., Brożyna, M., Junka, A., Shavandi, A., & Podstawczyk, D. (2022). 4D printing of patterned multimaterial magnetic hydrogel actuators. *Additive Manufacturing*, 49, 102506. <https://doi.org/10.1016/j.addma.2021.102506>

- [10] Kokol, V., Pottathara, Y. B., Mihelčič, M., & Perše, L. S. (2021). Rheological properties of gelatine hydrogels affected by flow- and horizontally-induced cooling rates during 3D cryo-printing. *Colloids and Surfaces A: Physicochemical and Engineering Aspects*, 616, 126356. <https://doi.org/10.1016/j.colsurfa.2021.126356>
- [11] Imura, Y., Hogan, R. M. C., & Jaffe, M. (2014). Dry spinning of synthetic polymer fibers. Advances in Filament Yarn Spinning of Textiles and Polymers, 187–202. <https://doi.org/10.1533/9780857099174.2.187>
- [12] Turek, K., & Opila, J. (1990). Magnetic fibers. *Journal of Magnetism and Magnetic Materials*, 83(1–3), 279–280. [https://doi.org/10.1016/0304-8853\(90\)90515-r](https://doi.org/10.1016/0304-8853(90)90515-r)
- [13] Banerjee, H., Leber, A., Laperrousaz, S., La Polla, R., Dong, C., Mansour, S., Wan, X., & Sorin, F. (2023). Soft multimaterial magnetic fibers and textiles. *Advanced Materials*, 35(33). <https://doi.org/10.1002/adma.202212202>
- [14] Wu, S., Hu, W., Ze, Q., Sitti, M., & Zhao, R. (2020). Multifunctional Magnetic Soft Composites: A Review. *Multifunctional Materials*, 3(4), 042003. <https://doi.org/10.1088/2399-7532/abcb0c>
- [15] Derby, N., & Olbert, S. (2010). Cylindrical magnets and ideal solenoids. *American Journal of Physics*, 78(3), 229–235. <https://doi.org/10.1119/1.3256157>
- [16] Maldonado-Camargo, L., Unni, M., & Rinaldi, C. (2017). Magnetic characterization of iron oxide nanoparticles for biomedical applications. *Methods in Molecular Biology*, 47–71. https://doi.org/10.1007/978-1-4939-6840-4_4
- [17] Dillard, D. A., Mukherjee, B., Karnal, P., Batra, R. C., & Frechette, J. (2018). A review of Winkler's foundation and its profound influence on adhesion and soft matter applications. *Soft Matter*, 14(19), 3669–3683. <https://doi.org/10.1039/c7sm02062g>
- [18] Kurowiak, J., Kaczmarek-Pawelska, A., Mackiewicz, A., Baldy-Chudzik, K., Mazurek-Popczyk, J., Zaręba, Ł., Klekiel, T., & Będziński, R. (2022). Changes in the mechanical properties of alginate-gelatin hydrogels with the addition of *Pygeum africanum* with potential application in urology. *International Journal of Molecular Sciences*, 23(18), 10324. <https://doi.org/10.3390/ijms231810324>
- [19] Liu, G., & Zhao, X. (2005). Electromechanochemical Behavior of Gelatin Hydrogel Under Electric Field. *Journal of Macromolecular Science, Part A*, 42, 51 - 59. <https://doi.org/10.1081/MA-200040958>.
- [20] Khosravi Maleki, F., KM Nasution, M., Gok, M. S., & Arab Maleki, V. (2022). An experimental investigation on mechanical properties of Fe₂O₃ microparticles reinforced polypropylene. *Journal of Materials Research and Technology*, 16, 229–237. <https://doi.org/10.1016/j.jmrt.2021.11.104>
- [21] Grothe, T., Briemann, J., & Ehrmann, A. (2016). PEO as spinnable polymer and spinning-agent for non-spinnable materials. In *Aachen-Dresden-Denkendorf International Textile Conference 2016*.
- [22] Lei, I. M., Sheng, Y., Lei, C. L., Leow, C., & Huang, Y. Y. (2022). A hackable, multi-functional, and modular extrusion 3D printer for soft materials. *Scientific Reports*, 12(1). <https://doi.org/10.1038/s41598-022-16008-6>

- [23] Du, Z., Ai, J., Zhang, X., Ma, Z., Wu, Z., Chen, D., Tao, G., & Su, B. (2020). Stretchable electromagnetic fibers for self-powered mechanical sensing. *Applied Materials Today*, 20, 100623. <https://doi.org/10.1016/j.apmt.2020.100623>
- [24] Wang, W., Ka, S. G., Pan, Y., Sheng, Y., & Huang, Y. Y. (2023). Biointerface fiber technology from electrospinning to inflight printing. *ACS Applied Materials & Interfaces*. <https://doi.org/10.1021/acsami.3c10617>
- [25] Chatterjee, K., & Ghosh, T. K. (2019). 3D printing of Textiles: Potential Roadmap to printing with fibers. *Advanced Materials*, 32(4). <https://doi.org/10.1002/adma.201902086>
- [26] Labowska, M. B., Cierluk, K., Jankowska, A. M., Kulbacka, J., Detyna, J., & Michalak, I. (2021). A Review on the Adaption of Alginate-Gelatin Hydrogels for 3D Cultures and Bioprinting. *Materials (Basel, Switzerland)*, 14(4), 858. <https://doi.org/10.3390/ma14040858>
- [27] Lee, K. Y., & Mooney, D. J. (2012). Alginate: Properties and biomedical applications. *Progress in Polymer Science*, 37(1), 106–126. <https://doi.org/10.1016/j.progpolymsci.2011.06.003>
- [28] Naghieh, S., Sarker, M., Sharma, N. K., Barhoumi, Z., & Chen, X. (2019). Printability of 3D printed hydrogel scaffolds: Influence of hydrogel composition and printing parameters. *Applied Sciences*, 10(1), 292. <https://doi.org/10.3390/app10010292>
- [29] Goudoulas, T.B. and Germann, N. (2017) Phase transition kinetics and rheology of gelatin-alginate mixtures, *Food Hydrocolloids*, 66, pp. 49–60. doi:10.1016/j.foodhyd.2016.12.018.
- [30] Doryab, A., Taskin, M. B., Stahlhut, P., Schröppel, A., Orak, S., Voss, C., Ahluwalia, A., Rehberg, M., Hilgendorff, A., Stöger, T., Groll, J., & Schmid, O. (2021). A bioinspired *in vitro* lung model to study particokinetics of nano-/microparticles under cyclic stretch and air-liquid interface conditions. *Frontiers in Bioengineering and Biotechnology*, 9. <https://doi.org/10.3389/fbioe.2021.616830>
- [31] Besarab, S. (2021). Artificial Extracellular Hydrogel Matrix for Treatment of Myocardial Infarction. Preprint available on ResearchGate. doi:10.13140/RG.2.2.35059.86569.

Attribution

Figure 1(a) was adapted from a figure in [31].

Figure 1(c) was adapted from lecture slides for module MLE4203 (Polymeric Biomedical Materials) at National University of Singapore by Dr Daria Andreeva (NUS Materials Science and Engineering).

All other media was created by myself or are screenshots from software I am licensed to use.

Files

Files useful for reproducing the software-based studies in this project can be found at my GitHub repository:

<https://github.com/lorcan2440/IIB-Project-Printing-Magnetic-Hydrogels>

(8) Appendix

8.1. Appendix I: Abbreviations used in this Report

3D	three dimensional	MBSC	microbiological safety cabinet
CAD	computer-aided design	PBS	phosphate-buffered saline
CUED	Cambridge Univ. Engineering Department	PEGDA	polyethylene glycol diacrylate
DI	deionised (water)	PEO	polyethylene oxide
DMF	<i>N,N</i> -dimethylformamide	PS	polystyrene
ECM	extracellular matrix	PU	Polyurethane
HEPA	high-efficiency particulate absorbing	SPION	superparamagnetic iron oxide nanoparticles
LCST	lower critical solution temperature	UCST	upper critical solution temperature
		UDL	uniformly distributed load

8.2. Appendix II: Predicted Young's Moduli of Gelatin-Alginate Hydrogels

Data was extracted from Table 1 in [18], excluding the last '30%, 65%' and 'human urethra' rows due to being an outlier and irrelevant respectively. Using Python's `scikit-learn` library, a 2nd order (quadratic) linear regression was performed without regularisation on the full dataset to produce the model represented by the curved surface below. The model attained a root mean squared error of 0.98 MPa. The two data points marked in red are for (6% gelatin, 1% alginate) and (2% gelatin, 0.333% alginate), evaluated as 0.57 MPa and 1.55 MPa respectively, for two specific compositions tested in this project.

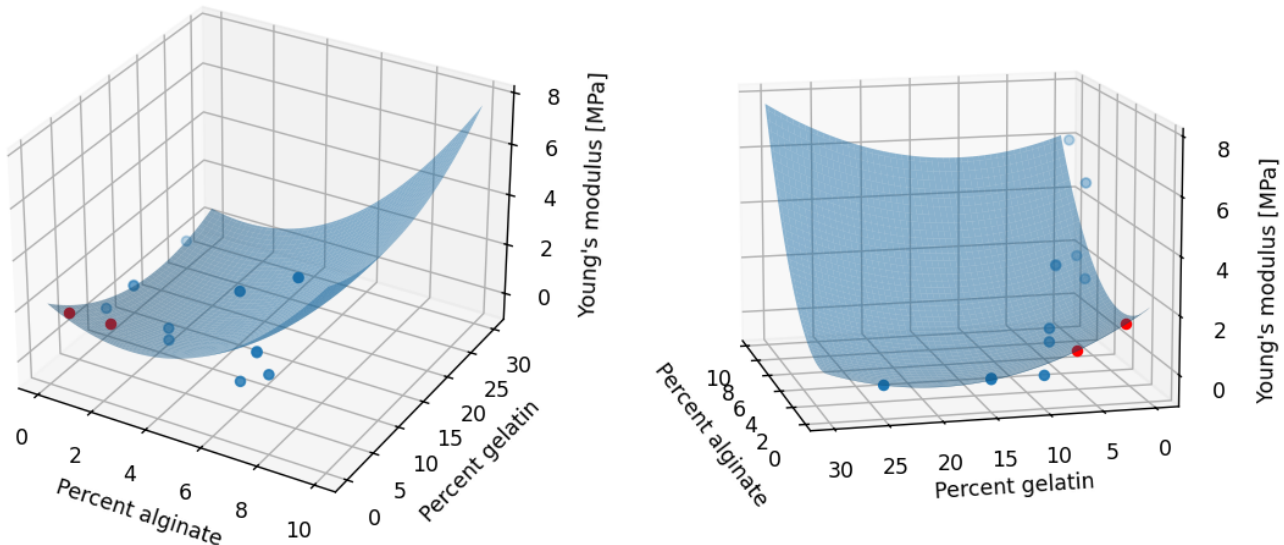


Fig. 24. Best-fit surface for elastic moduli of gelatin-alginate hydrogels. Made in `matplotlib`.

8.3. Appendix III: Robot Arm Code for Automated Wet Spinning (Python 3)

```

import os
import sys
import time
import threading

# import the uArm robot arm library
sys.path.append(os.path.join(os.path.dirname(__file__), "../.."))
from uarm.wrapper import SwiftAPI # robot arm library

# editable parameters
DEFAULT_POSITION = [250, 0, 115]
MOTION_RANGE = 8 # width of frame in mm to spin the fibres over
PRINTING_SPEED = 30 # rate of movement of robot arm from side to side
PRINTING_AXIS = 'y' # direction of movement
PRINT_TIME = 99999 # endless movement

# connect to the robot
swift = SwiftAPI(filters={"hwid": "USB VID:PID=2341:0042"})
swift.waiting_ready(timeout=3)
device_info = swift.get_device_info()
print(device_info)
firmware_version = device_info["firmware_version"]
if firmware_version and not firmware_version.startswith(("0.", "1.", "2.", "3.")):
    swift.set_speed_factor(0.0005)
swift.set_mode(0)

# move to default position
print('Moving to default position.')
swift.set_position(*DEFAULT_POSITION, speed=1000, wait=True)

# allow manual setting of the z-axis position (height above reference point in mm)
print('Minimum allowed z = -25 mm. Maximum allowed z = 160 mm.')
while True:
    pos = swift.get_position(wait=True, timeout=None, callback=None)
    print(f'Current (x, y, z) position (mm): {pos}.')
    entry = input("Adjust Z-axis position by how much (mm)? Press enter to continue. ")
    if entry == '':
        break
    else:
        try:
            new_z = pos[2] + float(entry)
            swift.set_position(pos[0], pos[1], new_z, speed=1000, wait=True)
        except (ValueError, TypeError):
            print("Invalid entry. Please enter a number to change the z-coordinate by in mm.")
            continue

# confirm ready to start print
pos = swift.get_position(wait=True, timeout=None, callback=None)
entry = input(f'Current z-axis position: {pos[2]}. Ready to start fibre printing, press "y" to go or anything else to exit. ')
if entry.lower() != 'y':
    print("Ending program.")
    exit(code=0)

```

```

def move_robot():
    i = 0
    t_start = time.time()
    while time.time() - t_start < PRINT_TIME:
        print(f'Starting pass {i+1}.')
        # move to other side
        if PRINTING_AXIS == 'x':
            swift.set_position(pos[0] - MOTION_RANGE, pos[1], pos[2], speed=PRINTING_SPEED,
                                wait=True)
        elif PRINTING_AXIS == 'y':
            swift.set_position(pos[0], pos[1] - MOTION_RANGE, pos[2], speed=PRINTING_SPEED,
                                wait=True)
        # move back
        swift.set_position(pos[0], pos[1], pos[2], speed=PRINTING_SPEED, wait=True)
        i += 1

if __name__ == '__main__':
    robot_thread = threading.Thread(target=move_robot, daemon=True)
    robot_thread.start()
    robot_thread.join(timeout=PRINT_TIME)
    print(f'Fibre printing complete after {PRINT_TIME} seconds. Moving to default position.')
    swift.set_position(*DEFAULT_POSITION, speed=1000, wait=True)

```

8.4. Appendix IV: Risk Assessment Retrospective

Before commencing this project, a range of risks were identified arising from electric shocks, chemical hazards, robotic actuators, biological hazards, thermal hazards and ergonomic factors from display screen equipment (DSE) in a risk assessment submitted to the CUED Safety Office. In response to this, training was undertaken to proactively reduce the risk of harm while working in the Containment Level 1 (CL1) biolab and Module 1 at the Nanoscience Centre:

- Read the OHSS guidance for safely working with some of the named hazards above.
- Completed a formal risk assessment of chemical hazards using the CUED Risk Assessment Assessor app, including a CoSSH assessment of the chemicals involved.
- Read and understood the SDS for all chemicals prior to their use in the project.
- Completed the Chemical Safety Training course exercise on Moodle.
- Attended an introductory Biological Safety Training seminar by Dr Thierry Savin.
- Attended a Chemical Safety Awareness seminar by Sean Whelan.

Many of these measures were successful in preventing accidents while working in the biolab. The identified risks were realistic and accounted for in practice throughout the project. Although working in an environment with cell cultures, I did not work with cells myself in this project, so this risk was not relevant to experimental work and was unnecessarily included in the original risk assessment. Otherwise, the risk assessment captured the real risks involved in the projects accurately, resulting in no major issues, so I retrospectively consider the assessment a success.